

# Global application of a regional frequency analysis on extreme sea levels

Authors: Thomas P. Collings<sup>1</sup>, Niall D. Quinn<sup>1</sup>, Ivan D. Haigh<sup>1,2</sup>, Joshua Green<sup>1,2</sup>, Izzy Probyn<sup>1</sup>, Hamish Wilkinson<sup>1</sup>, Sanne Muis<sup>3,4</sup>, William V. Sweet<sup>5</sup>, Paul D. Bates<sup>1,6</sup>

## Affiliations of Authors:

1. Fathom, Floor 2, Clifton Heights, Clifton, Bristol, UK. BS8 1EJ

2. School of Ocean and Earth Science, University of Southampton, National Oceanography Centre, European Way, Southampton SO14 3ZH

3. Deltares, Delft, Netherlands

4. Institute for Environmental Studies (IVM), Vrije Universiteit Amsterdam, Amsterdam, Netherlands

5. National Oceanic and Atmospheric Administration, National Ocean Service, Silver Spring, MD, United States

6. School of Geographical Sciences, University of Bristol, Bristol, UK

Correspondence to: [t.collings@fathom.global](mailto:t.collings@fathom.global)

26 **Abstract**

27 Coastal regions face increasing threats from rising sea levels and extreme weather events,  
28 highlighting the urgent need for accurate assessments of coastal flood risk. This study  
29 presents a novel approach to estimating global Extreme Sea Level (ESL) exceedance  
30 probabilities, using a Regional Frequency Analysis (RFA) approach. The research combines  
31 observed and modelled hindcast data to produce a high-resolution (~1 km) dataset of ESL  
32 exceedance probabilities, including wave setup, along the entire global coastline, excluding  
33 Antarctica.

34  
35 The methodology presented in this paper is an extension of the regional framework from  
36 Sweet et al., (2022), with innovations made to incorporate wave setup and apply the  
37 method globally. Water level records from tide gauges and a global reanalysis of tide and  
38 surge levels are integrated with a global ocean wave reanalysis. Subsequently, these data  
39 are regionalised, normalised, and aggregated, and then fit with a Generalised Pareto  
40 distribution. The regional distributions are downscaled to the local scale using the tidal  
41 range at every location along the global coastline, obtained through a global tide model. The  
42 results show 8cm of positive bias at the 1-in-10-year return level, when compared against  
43 individual tide gauges.

44  
45 The RFA approach offers several advantages over traditional methods, particularly in regions  
46 with limited observational data. It overcomes the challenge of short and incomplete  
47 observational records by substituting long historical records with a collection of shorter but  
48 spatially distributed records. This spatially distributed data not only retains the volume of  
49 information but also addresses the issue of sparse tide gauge coverage in less populated  
50 areas and developing nations. The RFA process is illustrated using Cyclone Yasi (2011) as a  
51 case study, demonstrating how the approach can improve the characterisation of ESLs in  
52 regions prone to tropical cyclone activity.

53  
54 In conclusion, this study provides a valuable resource for quantifying global coastal flood  
55 risk, offering an innovative global methodology that can contribute to preparing for, and  
56 mitigating against, coastal flooding.

57

58 **Plain language summary**

59 Coastal areas are at risk of flooding from rising sea levels and extreme weather events. This  
60 study uses a new way to figure out how likely coastal flooding is around the world. The  
61 method uses data from observations and computer models to create a detailed map of  
62 where these floods might happen at the coast. The approach can predict flooding in areas  
63 where there is little or no data. The results can be used to help get ready for and prevent  
64 this type of flooding.

65

66

## 67 **1. Introduction**

68 Flooding provides one of the greatest threats to coastal communities globally, causing  
69 devastating impacts to affected regions. Notable events which have caused significant  
70 coastal flooding in recent years include: Cyclone Amphan (2020), which struck the Bay of  
71 Bengal producing a storm surge of up to 4.6m along the coast of Western Bengal, killing 84  
72 people, and causing total losses over 13 billion USD (India Meteorological Department,  
73 2020; Kumar et al., 2021); Hurricane Harvey (2017), the second most costly hurricane to hit  
74 the US after Katrina (2005), which impacted 13 million people, hitting the state of Texas  
75 with a maximum storm surge of 3.8m (Amadeo, 2019); and Typhoon Jebi (2018), driving  
76 storm surges of over 3m in Osaka Bay, Japan, combined with wave action which led to  
77 flooding exceeding 5m above mean sea level (Mori et al., 2019). Approximately 10% of the  
78 world's population (768 million people) live below 10m above mean sea level (McGranahan  
79 et al., 2007, Nicholls et al., 2021). Coastal flooding is expected to increase dramatically into  
80 the future, predominantly caused by sea-level rise (Calafat et al., 2022, Taherkhani et al.,  
81 2020), and compounded by continued growth and development in coastal populations  
82 (Neumann et al., 2015). Therefore, continuing to improve the understanding of coastal  
83 flooding is vital.

84 Coastal floods are driven by extreme sea levels, which arise as combinations of: (1)  
85 astronomical tides; (2) storm surges (driven by tropical and extra-tropical cyclones) and  
86 associated seiches; (3) waves, especially setup and runup; and (4) relative mean sea level  
87 changes (including sea-level rise and vertical land movement). Risk assessments of coastal  
88 flooding require high-quality and high-resolution flood hazard data, typically in the form of  
89 flood inundation maps. Inundation maps are usually derived from hydraulic models, which  
90 use high resolution extreme sea level (ESL) exceedance probabilities as a key input (e.g.,  
91 (Bates et al., 2021, Mitchell et al., 2022). The development of coastal inundation maps is  
92 reliant on coastal boundary conditions points that vary in resolution depending on  
93 application. Previous studies (e.g., (Barnard et al., 2019)) have used 100m resolution at local  
94 scales, while regional studies (e.g., (Bates et al., 2021, Environment Agency, 2018)) have  
95 employed resolutions between 500m and 2km.

96 Traditional methods for computing ESL exceedance probabilities involve extreme value  
97 analysis of measurements from individual tide gauges or wave buoys. However, long,

98 complete records spanning numerous decades are necessary to obtain robust estimates of  
99 ESL return levels (Coles, 2001). The Global Extreme Sea Level Analysis (GESLA-3) database  
100 provides sea level records for over 5,000 tide gauge stations (Haigh et al., 2021), but these  
101 tide gauges still cover only a small fraction of the world's coastlines. Wave buoys are even  
102 more sparse, largely restricted to the Northern Hemisphere and long historical records are  
103 marred by discontinuities (Timmermans et al., 2020). Even in areas with relatively high tide  
104 gauge or wave buoy density, there are still large expanses of coastline which remain  
105 ungauged. While rare extreme weather events (such as intense tropical cyclones (TCs)) are  
106 often many hundreds of kilometres in size, the precise impact of the corresponding ESL can  
107 often be highly localised (Irish et al., 2008), meaning the peak surge occurs in an ungauged  
108 location. The particular locale of peak surge for an event is determined by storm  
109 characteristics, local bathymetry and coastal geography, amongst other factors (Shaji et al.,  
110 2014). Therefore, relying on past observation-based analyses of ESL exceedance  
111 probabilities to characterise return levels across a region will likely lead to the under  
112 representation of rare extreme events. Finally, another limitation is that many previous  
113 analyses of ESL exceedance probabilities consider the still water level component (i.e., tide  
114 plus storm surge) separately from the wave set up and run up (Haigh et al., 2016, Muis et  
115 al., 2016, Ramakrishnan et al., 2022).

116 One solution to overcome sparse datasets is to use ESL hindcasts created by state-of-the-art  
117 models. These include regional (e.g., (Andrée et al., 2021; Siah Sarani et al., 2021; Tanim and  
118 Akter, 2019)) or global tide-surge (such as Deltares' Global Tide Surge Model v3.0 (hereafter  
119 referred to as GTSM; (Muis et al., 2020)) or wave models (e.g., (Liang et al., 2019))). These  
120 are used to fill the spatial and temporal gaps in the observation records via historical  
121 reanalysis simulation. However, their ability to accurately capture extreme events is  
122 hampered by the atmospheric forcing data that is used to drive the models, as reanalysis  
123 products like ERA5 (Hersbach et al., 2020) commonly contain biases in representing  
124 meteorological extremes such as TCs (Slocum et al., 2022), leading to an underestimation of  
125 event intensity. Furthermore, the time period captured in reanalysis products is not  
126 adequate to represent the characteristics (e.g., frequencies) of particularly rare events such  
127 as intense TCs. To overcome this limitation, some studies have used synthetic event

128 datasets representing TC activity over many thousands of years (e.g., (Dullaart et al., 2021,  
129 Haigh et al., 2014)) however this approach is computationally expensive.

130 An alternative and less computationally demanding solution that helps address some of the  
131 problems inherent in estimating ESLs around the world's coastlines from the observational  
132 record, is regional frequency analysis (RFA). The RFA methodology was originally developed  
133 to estimate streamflow within a hydrological context (e.g., (Hosking & Wallis, 1997))but has  
134 since been used in many applications requiring extreme value analysis of meteorological  
135 parameters including coastal storm surge (e.g., (Arns et al., 2015, Bardet et al., 2011, Weiss  
136 & Bernardara, 2013)) and extreme ocean waves (e.g., (Campos et al., 2019, Lucas et al.,  
137 2017, Vanem, 2017)). The principle of an RFA is founded on the basis that a homogenous  
138 region can be identified, throughout which similar meteorological forcings and resultant  
139 storm surge or wave events could occur, even if the extreme events have not been seen in  
140 part of that region in the historical record (Hosking and Wallis, 1997). RFA has been used on  
141 a regional scale to produce coastal ESL exceedance probabilities including: France  
142 (Andreevsky et al., 2020; Hamdi et al., 2016); the US coastline (Sweet et al., 2022); Northern  
143 Europe (Frau et al., 2018); US coastal military sites (Hall et al., 2016); and the Pacific Basin  
144 (Sweet et al., 2020). However, an RFA approach has not (to our knowledge) been applied  
145 globally.

146 The overall aim of this paper is to, for the first time, apply an RFA approach to estimate ESL  
147 exceedance probabilities, including wave setup, along the entire global coastline. These  
148 exceedance probabilities aim to better characterise ESLs driven by rare, extreme events,  
149 such as those from TCs, which are poorly represented in the historical record. Uniquely, this  
150 study uses both measured and hindcast datasets; includes tides, storm surges, and wave  
151 setup; and calculates exceedance probabilities at high resolution (1 km) globally. The  
152 specific objectives of this paper are to:

- 153 (1) develop and apply the RFA globally (excluding Antarctica), utilising both  
154 observational tide gauge, and modelled hindcast sea level and wave records;
- 155 (2) illustrate how the RFA methodology improves the representation of rare extreme  
156 events in the ESL exceedance probabilities using cyclone Yasi, which impacted the  
157 Australian coastline in 2011, as a case study;

- 158 (3) validate the RFA against exceedance probabilities estimated from the GESLA-3 global  
159 tide gauge database; and
- 160 (4) Finally, quantify how much the RFA increases the estimation of ESL exceedance  
161 probabilities in areas prone to TC activity when compared to single site analysis,  
162 using hindcast datasets (Muis et al., 2020) and (Dullaart et al., 2021).

163 This paper is laid out as follows: The datasets used are described in Section 2. The  
164 methodology is detailed in Section 3, addressing objective 1. Results and validation are  
165 described in Section 4, addressing objectives 2, 3, and 4. A discussion of the key findings and  
166 conclusions are then given in Sections 5 and 6, respectively.

167

## 168 2. Data

169 We use seven primary sources of data in this study, namely: (1) still sea-level observations  
170 contained in the GESLA-3 tide gauge dataset; (2) global still sea-level simulations from the  
171 GTSM hindcast based on the ERA5 climate reanalysis; (3) tidal predictions from the FES2014  
172 finite element hydrodynamic model; (4) significant wave heights derived from the ERA5  
173 climate reanalysis; (5) mean dynamic topography from HYBRID-CNES-CLS18-CMEMS2020;  
174 (6) Copernicus DEM to create a global coastline dataset; and (7) the COAST-RP dataset from  
175 (Dullaart et al., 2021) to validate the RFA methodology. These seven datasets are described  
176 in turn below.

177 Still sea level records are assembled from the GESLA-3 (Global Extreme Sea Level Analysis)  
178 tide gauge dataset version 3 (Caldwell et al., 2015, Haigh et al., 2021). The GESLA-3 dataset  
179 includes high-frequency water level time series from over 5,000 tide gauges around the  
180 globe, collated from 36 international and national providers. Data providers have differing  
181 methods of quality control, however each record was visually assessed by the authors of the  
182 GESLA-3 dataset and graded as either: (i) no obvious issues; (ii) possible datum issues; (iii)  
183 possible quality control issues; or (iv) possible datum and quality control issues. Only  
184 records with no obvious issues were used in this study.

185 As discussed in Section 3, the hindcast, GTSM-ERA5 is used in all areas which are not  
186 covered by tide gauge observations. GTSM is a depth-averaged hydrodynamic model built

187 using the DELFT-3D hydrodynamic model, which makes use of an unstructured, global,  
188 flexible mesh with no open boundaries (Muis et al., 2020). The model has a coastal  
189 resolution of 2.5km (1.25km in Europe), and a deep ocean resolution of 25km. The GTSM-  
190 ERA5 dataset spans the period 1979-2018 and is developed by forcing GTSM with hourly  
191 fields of ERA5 10-metre wind speed and atmospheric pressure (Hersbach et al., 2020).  
192 GTSM-ERA5 has a 10-minute temporal resolution and provides a timeseries at locations  
193 approximately every 50km along the coastline (10km in Europe). Validation carried out by  
194 Muis et al. (2020) shows that the dataset performs well against observations of annual  
195 maximum water level, exhibiting a mean bias of -0.04 m and a mean absolute percentage  
196 error of 14%.

197 We use the FES2014 tidal database to generate tidal timeseries at GTSM-ERA5 locations and  
198 RFA output locations. The RFA output resolution is much higher than the output resolution  
199 of GTSM-ERA5, which is why FES2014 is used instead. FES2014 is a finite element  
200 hydrodynamic model which combines data assimilation from satellite altimetry and tide  
201 gauges (Lyard et al., 2021). The model solves the barotropic tidal equations, as well as the  
202 effects from self-attraction and loading. The gridded resolution of the output is  $1/16^\circ$ . The  
203 model was extensively validated against tide gauges, satellite altimeter observations, and  
204 alternative global tide models by Lyard et al. (2021) and was found to have an improved  
205 variance reduction in nearly all areas, especially in shallow water regions. The Python  
206 package distributed with the FES2014 data (<https://github.com/CNES/aviso-fes>) was used to  
207 simulate tidal timeseries.

208 To calculate wave set up we use significant wave heights ( $H_s$ ) from the ERA5 reanalysis  
209 (Hersbach et al., 2020), covering the period 1979 to 2020. The spatial resolution of the ERA5  
210 wave model output is  $0.5^\circ \times 0.5^\circ$ , and the temporal resolution is hourly. Independent  
211 validation of hourly  $H_s$  performed by (Wang & Wang, 2022) finds little bias in the dataset (-  
212 0.058 m), however the authors go on to conclude that  $H_s$  of extreme waves tends to be  
213 underestimated (by 7.7% in the 95% percentile), a conclusion supported by (Fanti et al.,  
214 2023).

215 We use mean dynamic topography (MDT) to convert water levels from mean sea level as  
216 measured by tide gauges to mean sea level as referenced by a geoid, for use in subsequent  
217 future studies involving inundation assessments using hydraulic modelling. MDT describes



218 the change in sea surface height due to the effects of the winds and currents in the ocean.  
219 Digital elevation models (DEMs), a key input to hydraulic models, typically use a geoid as a  
220 vertical datum. A geoid is an equipotential surface of mean sea level under the sole effect of  
221 gravity, in the absence of land masses, currents and tides (Bingham and Haines, 2006). To  
222 convert water levels from tide gauge mean sea level to the geoid mean sea level, the  
223 HYBRID-CNES-CLS18-CMEMS2020 MDT dataset is used (Mulet et al., 2021). The spatial  
224 resolution of this dataset is  $0.125^\circ \times 0.125^\circ$ . Errors associated with this dataset are largely  
225 caused by the input satellite altimetry data and can be up to 10 cm in some areas. The MDT  
226 at the shoreline is illustrated in the Appendix Fig. A1.

227 The Copernicus 30m DEM (European Space Agency, 2021) is used to create a high-resolution  
228 global coastline. This is used to define the RFA output points at approximately 1 km intervals  
229 along the global coastline (excluding Antarctica), resulting in over 3.4 million points.

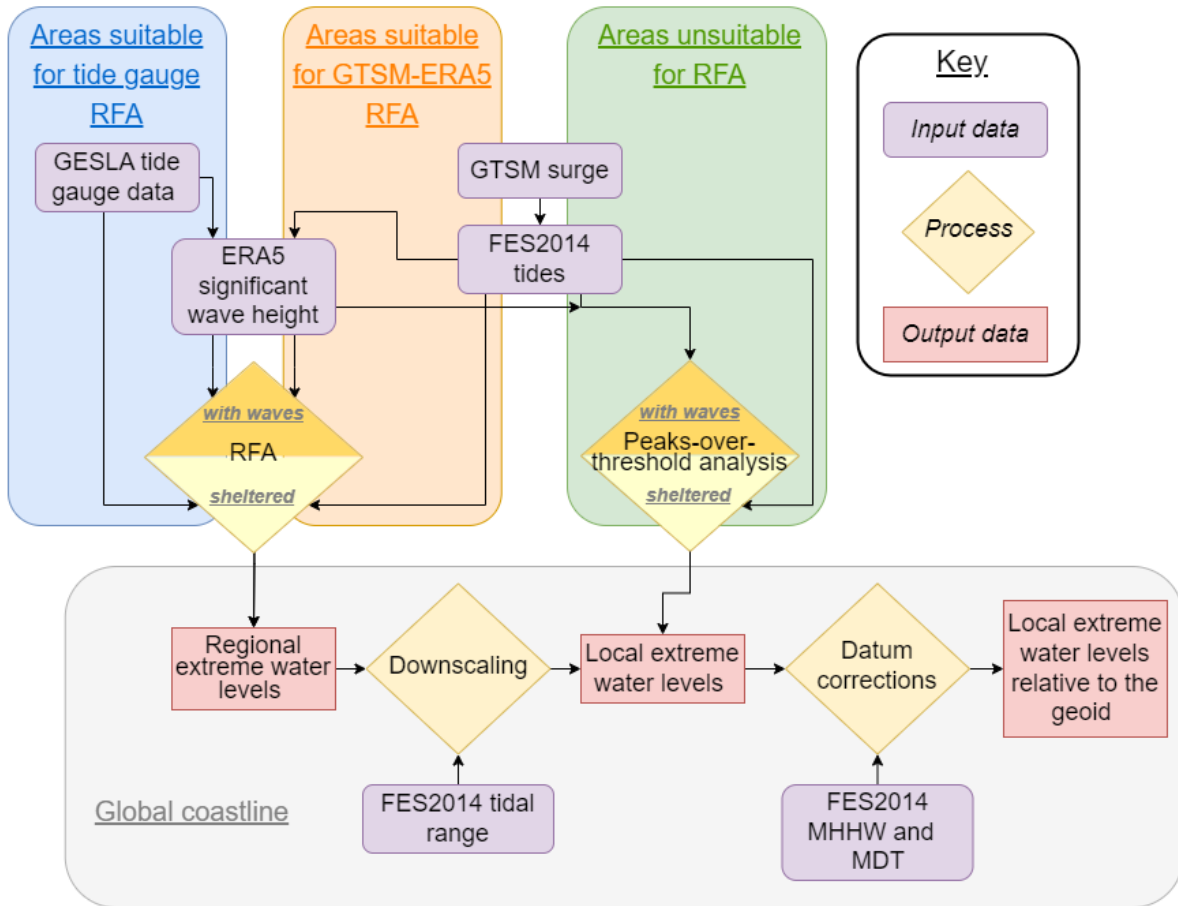
230 Finally, in addition to GTSM-ERA5, we use the COAST-RP dataset from (Dullaart et al., 2021)  
231 to validate the RFA methodology. COAST-RP uses the same hydraulic modelling framework  
232 as GTSM-ERA5 but simulates extra-tropical and tropical surge events separately using  
233 different forcing data. In areas prone to TC activity, synthetic TCs representing 3,000 years  
234 under current climate conditions are used from the STORM dataset (Bloemendaal et al.,  
235 2020). These synthetic TC model runs have been validated against observed IBTrACS-forced  
236 model runs, and found to show differences in ESLs at the 1 in 25 year return level of less  
237 than 0.1 m at 67% of the output locations in TC prone areas (Dullaart et al., 2021). In regions  
238 impacted only by extra-tropical storms, a 38-year timeseries of ERA5 data is used (Hersbach  
239 et al., 2020). The surge levels from each set of simulations are probabilistically combined  
240 with tides to result in a global database of dynamically modelled storm-tides.

241

### 242 3. Methods

243 The first objective of this study is to develop and apply an RFA approach globally,  
244 encompassing still water levels and wave set up. In Section 3.1 we describe the methods  
245 used to process the data used in this study. In Section 3.2 we layout the global application of  
246 the RFA approach using observational and modelled data. The methods used to validate the  
247 results are explained in Section 3.3.

248 An overview of our methodology is illustrated in Fig. 1. This study broadly follows the  
249 methodology of (Sweet et al., 2022) and applies an RFA to both tide gauge and GTSM-ERA5  
250 records. As such, the terms ‘water level record’ and ‘record location’ are used to describe  
251 both tide gauge records and GTSM-ERA5 data. The method can be summarised in five key  
252 steps: (i) collation and pre-processing of tide gauge, GTSM-ERA5, FES2014, and ERA5 Hs  
253 data; (ii) spatial discretisation of water level records into regions; (iii) application of the RFA  
254 to regional water level records (in areas unsuitable for an RFA (because there are less than 3  
255 gauges in a region, or the regional water levels records are heterogenous), a peaks-over-  
256 threshold analysis of individual GTSM-ERA5 water level records is used); (iv) conversion  
257 (downscaling) of RFA exceedance levels to local exceedance levels at the output coastline  
258 points, using FES2014 tidal range (in areas unsuitable for an RFA, nearest-neighbour  
259 interpolation is used to assign local exceedance levels); and (v) correction of bias and  
260 datums to convert water levels to geoid mean sea level, using FES2014 mean higher high  
261 water and global MDT (HYBRID-CNES-CLS18-CMEMS2020). The final section of the methods  
262 (vi) describes the validation techniques. These steps are described in detail below.



264

265 *Figure 1: Schematic flow diagram detailing the data sources and processes involved in producing a global set of extreme*  
 266 *water levels*

267 **3.1 Data processing**

268

269 The GESLA-3 dataset was filtered to sample appropriate input data by removing duplicates,  
 270 gauges located in rivers (away from the coast), and gauges that fail quality control checks  
 271 carried out by the authors of the dataset (such as suspected datum jumps). The surge  
 272 component of GTSM-ERA5 at each record location is isolated from the water level  
 273 timeseries using a tide only simulation and superimposed upon a tidal timeseries created  
 274 with FES2014, as the FES2014 tidal elevations performed better than those of GTSM in  
 275 initial testing against in-situ observation. The decision to use tides from FES2014 is further  
 276 supported by the conclusion from Muis et al., (2020), in which they state “It appears that  
 277 biases increase in regions with a high tidal range, such as the North Sea, northern Australia,  
 278 and the northwest of the United States and Canada, which could indicate that GTSM is  
 279 outperformed by the FES2012 model that was used to develop the GTSR dataset.” Tidal

280 timeseries were also computed at each of the coastline output locations for use in  
281 downscaling the regional outputs, and in the bias and datum corrections of the local ESL.

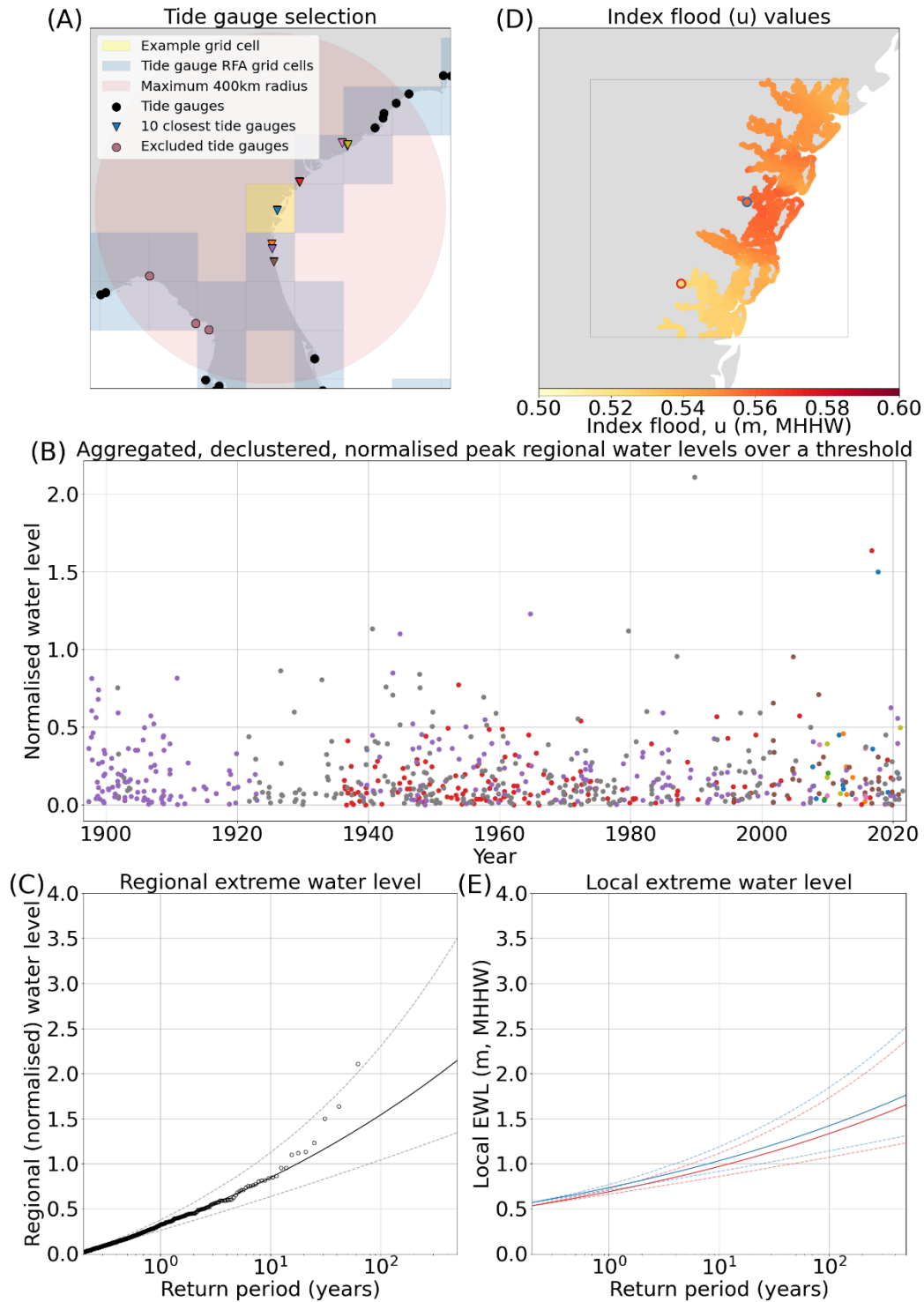
282 Wave setup is the static increase in water level attributed to residual energy remaining after  
283 a wave breaks (Dean and Walton, 2010), and therefore is only observed in areas exposed to  
284 direct wave action. In this study, wave setup is approximated as 20% significant wave height  
285 ( $H_s$ ) from the ERA5 reanalysis, following the recommendation from the review of numerous  
286 laboratory and field experiments ((Dean & Walton, 2010) and previous related studies  
287 (Bates et al., 2021; Vousdoukas et al., 2016). Wave setup is assigned to the nearest record  
288 location using a nearest-neighbour approach. Wave setup is assumed to be absent in  
289 sheltered areas (e.g., bays and estuaries). To account for this, the global coastline is  
290 classified as either sheltered or exposed, and the final extreme water levels are drawn from  
291 an RFA that is processed with or without wave setup added in. To classify the coastline, each  
292 coastline point is evaluated to determine if it is exposed from a minimum  $22.5^\circ$  angle over a  
293 fetch of 50km. A total of 16 equal angle transects are drawn, extending 50km from each  
294 coastline point. If two or more adjacent transects do not intersect with land, the coastline  
295 point is considered exposed. Applying wave setup using this approach is an obvious  
296 simplification that has been used for the ease of global application. In reality wave setup is  
297 impacted by local bathymetry and coastal geometry, as well as local wind and wave  
298 conditions. There are other more complex methods for estimating wave setup that  
299 incorporate some aspects of bathymetry and coastal geometry, such as Stockdon et al.  
300 (2006).

301 To process the RFA with wave setup, daily maximum wave setup is added to the daily  
302 highest water levels. Where tide gauge records fall outside of the temporal range of the  
303 ERA5 data, a copula-based approach was used to fit a simple statistical model between daily  
304 peak water levels and daily max  $H_s$ , providing a prediction of the daily max  $H_s$ . The RFA is  
305 then executed as described below. Tide gauges are assumed to be located in sheltered  
306 regions, such as bays and estuaries, thus tide gauge records are not impacted by wave  
307 setup.

### 308 3.2 Spatial discretisation of water level records into regions

309

310 Water level records are spatially clustered to form a potential pool from which regional  
311 exceedance levels can be characterised. To do this, the global coastline is divided into 1° by  
312 1° grid cells, which are used as the regions to apply the outputs for each RFA. All record  
313 locations within a 400km radius (same as (Hall et al., 2016) and (Sweet et al., 2022)) of the  
314 grid cell centroid that have at least 10 consecutive years of good (>90% completeness) data  
315 are identified (minimum of 3 water level records, maximum of 10 (same as Sweet et al.  
316 (2022))). This step is illustrated in Fig. 2A. Record locations which are geographically within  
317 range, but are separated by a large expanse of land, and thus likely forced by different  
318 storm patterns are removed from the record location selection. To achieve this, a line is  
319 drawn between the grid cell centroid and each record location. The land intersected by the  
320 line is divided, and the areas of land on either side of the line are summed. A ratio of the  
321 length of the line to the area of land segmented by the line is then calculated. A threshold of  
322 100 was empirically evaluated using expert judgement based on a number of test cases,  
323 above which records are removed from the grid cell analysis. This approach ensures that, for  
324 example, record locations located on the east coast of Florida (e.g., Mayport) are not  
325 grouped with those on the west coast (e.g., Cedar Key) when characterising regional growth  
326 curves, despite the relatively short straight-line distance between them. Fig. 2A exemplifies  
327 three tide gauges which have been excluded from possible selection despite lying within a  
328 400km radius to the grid cell centroid as the land that separates them is considerably large  
329 when compared to the distance. This spatial discretisation of regions results in a total of  
330 836 tide gauge records (with a mean record length of 17 years) and 18628 GTSM-ERA5  
331 records for use in the application of the RFA.

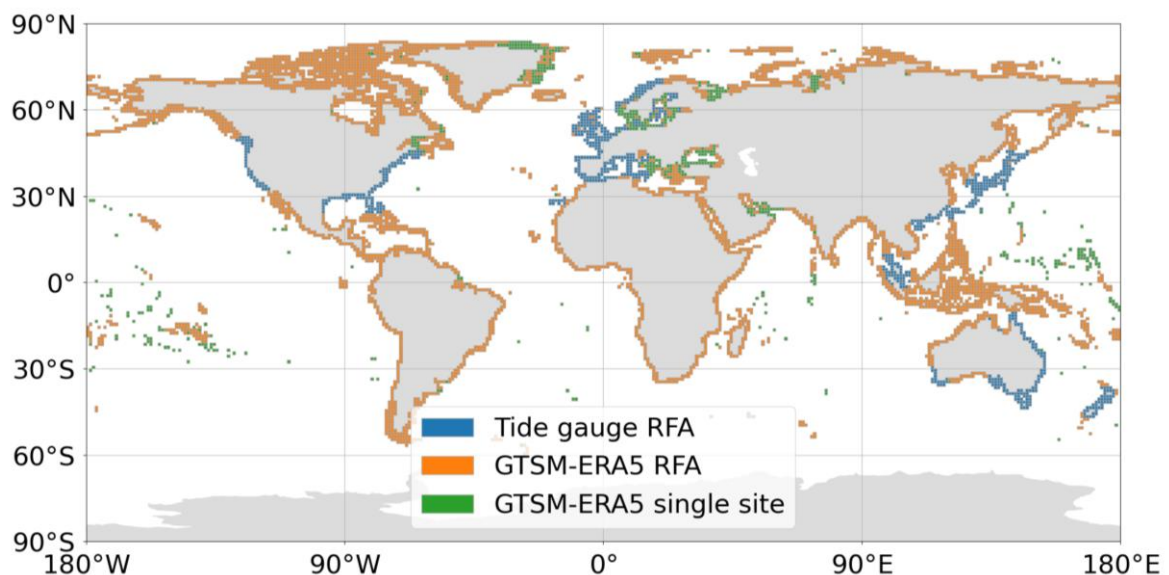


332

333 *Figure 2: Illustrating a selection of the steps through the RFA. (A) The 1° by 1° grid cells along the East Coast of the US,*  
 334 *along with the locations of the tide gauges, and the tide gauges selected for the RFA of the example grid cell. The tide*  
 335 *gauges excluded from possible selection by the distance/land area ratio are also indicated. (B) The aggregated, declustered,*  
 336 *normalised peak regional water levels over a threshold for each of the tide gauges used in the example grid cell. The colours*  
 337 *indicate peak water levels from the individual tide gauges in the region. (C) The regional extreme water levels, ascertained*  
 338 *by fitting a Generalised Pareto distribution to the data displayed in panel (B). (D) The index flood values of the example grid*  
 339 *cell, found by linearly interpolating the u value from the two closest tide gauges, and scaling by tidal range. The locations of*  
 340 *two coastline points used to produce local extreme water levels in panel E are also highlighted. (E) The local extreme water*  
 341 *level at two shoreline points inside the example grid cell, each with different index flood values as indicated in panel D.*

342 The RFA is preferentially applied to tide gauges in areas where the gauge density is sufficient  
343 (minimum 3 gauges within a 400km radius, same as (Hall et al., 2016) and (Sweet et al.,  
344 2022)). Outside of these areas, the RFA is implemented using data from GTSM-ERA5. In  
345 some regions, the density of homogenous record locations from GTSM-ERA5 is also too low  
346 for the RFA to function, in which case the ESL exceedance probabilities are interpolated  
347 from a single site peaks-over-threshold analysis of the nearest GTSM-ERA5 record location.  
348 The geographical locations of these areas are shown in Fig. 3. From the 5,975 global coastal  
349 grid cells, ESLs at 851 are computed using tide gauge data, 4,555 are calculated using an RFA  
350 of GTSM-ERA5 data, and 569 are calculated using GTSM-ERA5 data from the nearest record  
351 location.

352



353 *Figure 3: This map shows the global distribution the areas in which the tide gauge RFA is used, the GTSM-ERA5 RFA is used,*  
354 *and the areas which are interpolations of single site analysis from GTSM-ERA5.*

### 355 3.3 Application of the RFA

356

357 Tide gauge records are referenced to different vertical datums, so to ensure consistency, the  
358 mean over the most recent 19-year epoch is subtract from the water level record, and the  
359 timeseries is linearly detrended to the centre year of the most recent available epoch (2002-  
360 2020), resulting in 2011. GTSM-ERA5 records are referenced to MSL over the period of  
361 1986-2005, and so the timeseries are linearly detrended to reference the same tidal epoch  
362 as the tide gauge records, centred on 2011. Within each cluster of gauge (or model) records,

363 the water level time series are resampled to hourly resolution and converted to mean  
364 higher high water, defined as the mean daily highest water level over a 19-year epoch, to  
365 account for differences in tidal range between record locations. In the case of records with  
366 fewer than 19 years of data available the maximum continuous epoch is used instead.

367 Daily highest water level is determined from the hourly time series of each measured or  
368 modelled record. The time series are then declustered using a 4-day storm window to  
369 ensure event independence. This window length was used by Sweet et al., 2020 and Sweet  
370 et al., 2022, and is a similar length to the storms that cause surge events in the UK (Haigh et  
371 al., 2016). The index flood  $u$ , defined as the 98th percentile of the declustered daily highest  
372 water levels (Sweet et al., 2022), is used as the exceedance threshold at which to normalise  
373 the water level at each record location, as follows:

$$374 \quad \text{Normalised water level} = (\text{Observed exceedance water level} - u) / u \quad (\text{eq. 1})$$

375 The normalised datasets are then aggregated and further declustered to ensure only one  
376 peak water level is retained for each regional event. This is shown in Fig. 2B for an example  
377 grid cell. Following Hosking and Wallis (1997), a statistical heterogeneity test (H) is  
378 undertaken to ensure the homogeneity of the region. If the H-score is less than 2, then the  
379 region is considered sufficiently homogenous. If the H-score is greater than 2, then the  
380 furthest water level record from the grid cell centroid is removed from the region, and the  
381 test re-run. This process is repeated until the H-score is less than 2. In a minority of cases,  
382 the heterogeneity test fails due to an anomalous record that lies within the closest 3  
383 sampling locations to the grid cell centroid. In this instance the test is rerun, except after the  
384 furthest record is removed, all the remaining records are sequentially removed and  
385 replaced, until the H-score is less than 2.

386 After the region is confirmed to be homogenous, a Generalised Pareto distribution is fitted  
387 to the aggregated, declustered, normalised regional water levels using a penalised  
388 maximum likelihood method to estimate regional extreme water levels (REWLs). This is  
389 illustrated at an example in Fig. 2C. This is repeated for the aggregated regional water levels  
390 for each 1° by 1° grid cell. While theoretically correct, applying distribution fits to real world  
391 data can sometimes give unrealistic results, particularly in the estimation of the lower  
392 frequency space. In these cases, growth curve optimisation is undertaken to ensure the



393 output local extreme water levels are plausible in real world scenarios. To ensure  
394 consistency, an empirical threshold of 0.35 for the shape parameter is used to determine  
395 which curves will generate unrealistic extreme water levels. The empirical threshold of the  
396 shape parameter is determined based on expert judgement of plausible real world  
397 maximum surge heights in the low frequency events. To correct these curves, where this  
398 threshold is exceeded, we use the shape and scale parameters of the nearest grid cell which  
399 has a shape parameter less than 0.35. In total, 34 grid cells had their shape and scale  
400 parameters adjusted, mostly concentrated in the Gulf of Mexico and Japan.

### 401 3.4 Downscaling to local extreme water levels

402

403 Local extreme water levels (LEWLs) are then estimated from the regional growth curves  
404 using the following relationship:

$$405 \quad LEWL = (REWL * u) + u \quad (eq. 2)$$

406 for each coastal point along the coastline contained within the grid cell represented by the  
407 REWL. The index  $u$  is estimated at the coastline points using an inverse distance weighting  
408 interpolation of the  $u$  values for the two closest record locations, scaled by tidal range. This  
409 deviates from the methodology set out by Sweet et al., (2022), in which they recommend  
410 drawing  $u$  values from a linear regression of  $u$  against tidal range values from record  
411 locations across a region. We found this approach led to significant differences in LEWLs at  
412 record locations when compared to single site analysis of water level records, and hence  
413 have modified the methodology. Fig. 2D exhibits an example of the index flood for every  
414 shoreline point in an example grid cell. Tidal ranges are calculated as the difference  
415 between mean higher high water and mean lower low water. Tidal harmonics from FES2014  
416 are used to predict mean higher high water and mean lower low water at each coastline  
417 point. The index flood,  $u$ , is used to downscale the REWLs, which represent the ESL  
418 characteristics of the entire grid cell. LEWLs are output in the format of return levels for a  
419 range of exceedance probabilities. Two example LEWL curves are shown in Fig. 2E, which  
420 have been computed using different index flood values, as indicated in Fig. 2D.

### 421 3.5 Bias and datum corrections

422

423 The last stage of the LEWL calculation involved characterisation and removal of bias in the  
424 high frequency portion of the exceedance probability curves, relative to a single site analysis  
425 of water level records (within which we expect the high frequency water levels to be  
426 accurately modelled). Other surge RFA studies also concluded that the approach generally  
427 yields higher estimated surge heights when compared to single site analysis, because during  
428 the regionalisation process an extreme event that occurred in one location is assumed to  
429 have the same probability of occurring at another location within the homogeneous region.  
430 (Bardet et al., 2011; Sweet et al., 2022). Bias is quantified based on the divergence in the 1-  
431 in-1-year return period at each tide gauge/GTSM-ERA5 location and the corresponding  
432 LEWL predictions. This bias is used as a correction term and is removed from the LEWLs. As  
433 the density of the coastline points is much greater than the density of the tide  
434 gauges/model output locations, the correction term is interpolated across all coastal LEWL  
435 points based on correlation between monthly values of the 99<sup>th</sup> percentile of tidal  
436 elevations produced over a 3-year period centred on 2011, computed using FES2014 at the  
437 tide gauge/GTSM-ERA5 location and neighbouring coastline points. The mean bias  
438 correction across all gauges is 8 cm.

439 Datum corrections are applied to ensure the LEWLs are correctly referenced to a vertical  
440 datum which can be used for hazard assessment applications, such as inundation modelling.  
441 Inundation models utilise digital elevation models, which typically reference a geoid as the  
442 vertical datum. The output water levels from the RFA are transformed from mean higher  
443 high water to Mean Sea Level (MSL) by adding the approximation of mean higher high water  
444 (above MSL) from the FES2014 simulations to each of the boundary condition points. The  
445 corrected MDT dataset from (Mulet et al., 2021) is applied to convert water levels from MSL  
446 from the FES2014 model to the 'MSL' of a commonly used geoid, EGM08.

### 447 3.6 Validation methods

448

449 In this section we define a range of validation techniques used to address objectives 3 and 4.  
450 To validate the RFA ESLs against tide gauge records from GESLA (objective 3), a comparison  
451 is made against ESL exceedance probabilities calculated at the individual tide gauges used to  
452 inform the RFA. To quantify the degree to which the RFA approach improves the estimation

453 of ESL exceedance probabilities compared to single site analysis (objective 4), two  
454 assessments are made.

455 Firstly, the divergence between GTSM-ERA5 RFA ESL and GTSM-ERA5 single site ESL for the  
456 entire global coastline are quantified. These are then contrasted against the differences  
457 between return levels from GTSM-ERA5 (Muis et al., 2020) and COAST-RP (Dullaart et al.,  
458 2021). The comparison can then identify regions in which the historical ESLs are poorly  
459 represented due to the limited record lengths.

460 Secondly, a leave-one-out cross validation is undertaken using GTSM-ERA5 data. Leave-one  
461 out-cross validation aims to address the common issues involved with validating statistical  
462 models. One common method to validate models is split-sample validation, in which the  
463 data is split into two groups, a training set and a validation set, which are generally 70% and  
464 30% of the data respectively. The model is then trained on the larger set and validated  
465 against the smaller set. The drawbacks of this method include a highly variable validation  
466 error, due to the selection of the training and validation sets, as well as a validation error  
467 bias caused by training the model on only 70% of the available data (James et al., 2013).

468 Instead of using a 70/30 split of the data, leave-one-out cross validation uses a larger  
469 proportion of the data to train the model, while validating against a smaller sub-sample, but  
470 repeats this process multiple times to generate a robust validation. To do this, we identified  
471 1000 grid cells which use 10 GTSM-ERA5 records for the RFA and contain 3 GTSM-ERA5  
472 record locations inside the grid cell (and therefore the RFA can be used to directly estimate  
473 ESLs at the record locations). One of the GTSM-ERA5 records from inside the grid cell is  
474 removed from the RFA process, and the REWL is calculated using the 9 remaining gauges.  
475 The LEWL is then predicted at the record location which has been left out, using the index  
476 flood,  $u$  at the record location. These LEWLs are then contrasted with a single site analysis of  
477 the water level record that was removed from the RFA. The process is then repeated for the  
478 2 other GTSM-ERA5 record locations which lie within the grid cell. This means each of the  
479 1000 models is being tested three times, against 90% of the available data, thus giving a  
480 more robust realisation of the model when trained on 100% of the data.

481

## 482 4. Results

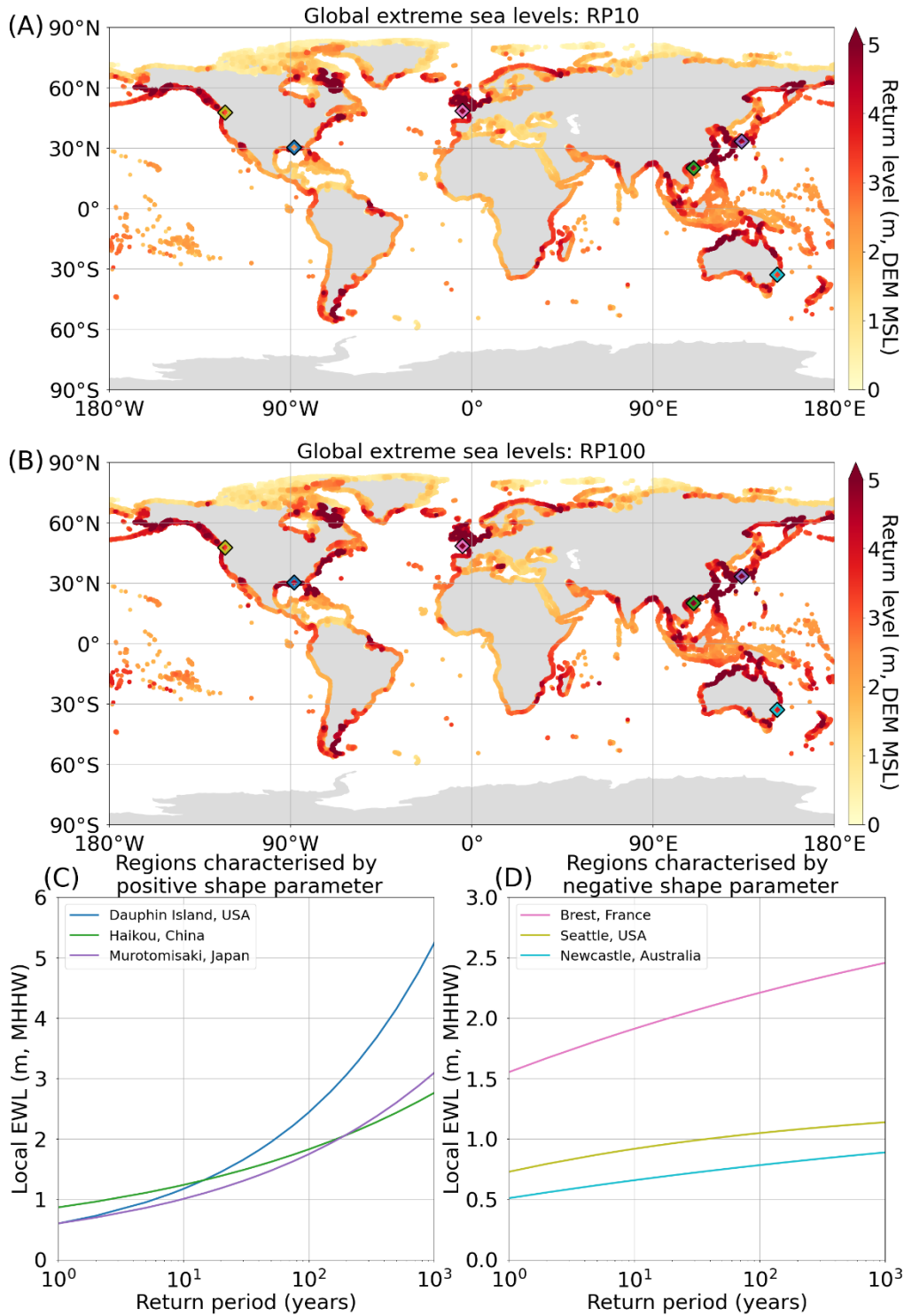
483 The results section is divided into four sub-sections. Section 4.1 presents the results of the  
484 global application of the RFA, showing both the global view of two return periods and the  
485 return levels for selected sites around the world. Section 4.2 illustrates how the RFA  
486 methodology improves the characterisation of rare extreme events using Cyclone Yasi  
487 (objective 2). In section 4.3 we validate the RFA against estimates of ESL from GESLA tide  
488 gauges (objective 3). Finally, in section 4.4 we quantify the improvements made by using an  
489 RFA approach when compared to a single site analysis of water levels (objective 4).

490

### 491 4.1 Global application of RFA

492 The final ESL exceedance probabilities (including wave setup) created at high resolution  
493 around the global coastline are displayed in Fig. 4, for the 1-in-10 and 1-in-100-year return  
494 periods. Both the 1-in-10 year (Fig. 4A) and 1-in-100 year (Fig. 4B) return periods show  
495 similar spatial patterns, with 1-in-100-year return periods exhibiting greater increases as  
496 expected in areas prone to TC activity (e.g., the Gulf of Mexico, Australia, Japan, and China).  
497 ESLs are higher in regions with large tidal ranges such as the Bay of Fundy, the Patagonia  
498 Shelf, the Bristol Channel in UK, the northern coast of France, and the northwest coast of  
499 Australia. The return levels for 6 select tide gauge locations, 3 of which are characterised by  
500 a positive and 3 of which are characterised by negative shape parameter from the  
501 Generalised Pareto distribution are shown in Fig. 4C and 4D respectively, relative to mean  
502 higher high water. The locations of the 6 tide gauges are indicated in both Fig. 4A and 4B.  
503 Regions exhibiting positive shape parameters are typically prone to TC activity and  
504 associated surge and wave events. As a result, these regions experience more significant  
505 increases in return levels at higher return periods than regions with negative shape  
506 parameters. Regions characterised by negative shape parameters have different drivers of  
507 ESL events, for instance extra-tropical storms surges or tide dominated ESLs (Sweet et al.,  
508 2020).

509



510

511 *Figure 4: The final global RFA results output at approximately 1km resolution along the entire global coastline (excluding*  
 512 *Antarctica) for RP10 (A) and RP100 (B). Return levels are referenced to DEM MSL, and so represent surge, waves and tide.*  
 513 *Return levels (relative to mean higher high water) for 6 tide gauges in regions characterised by either positive or negative*  
 514 *shape parameter of the Generalised Pareto distribution are shown in panels (C) and (D) respectively. The locations of the 6*  
 515 *tide gauges are indicated by the diamonds plotted on both panels (A) and (B).*

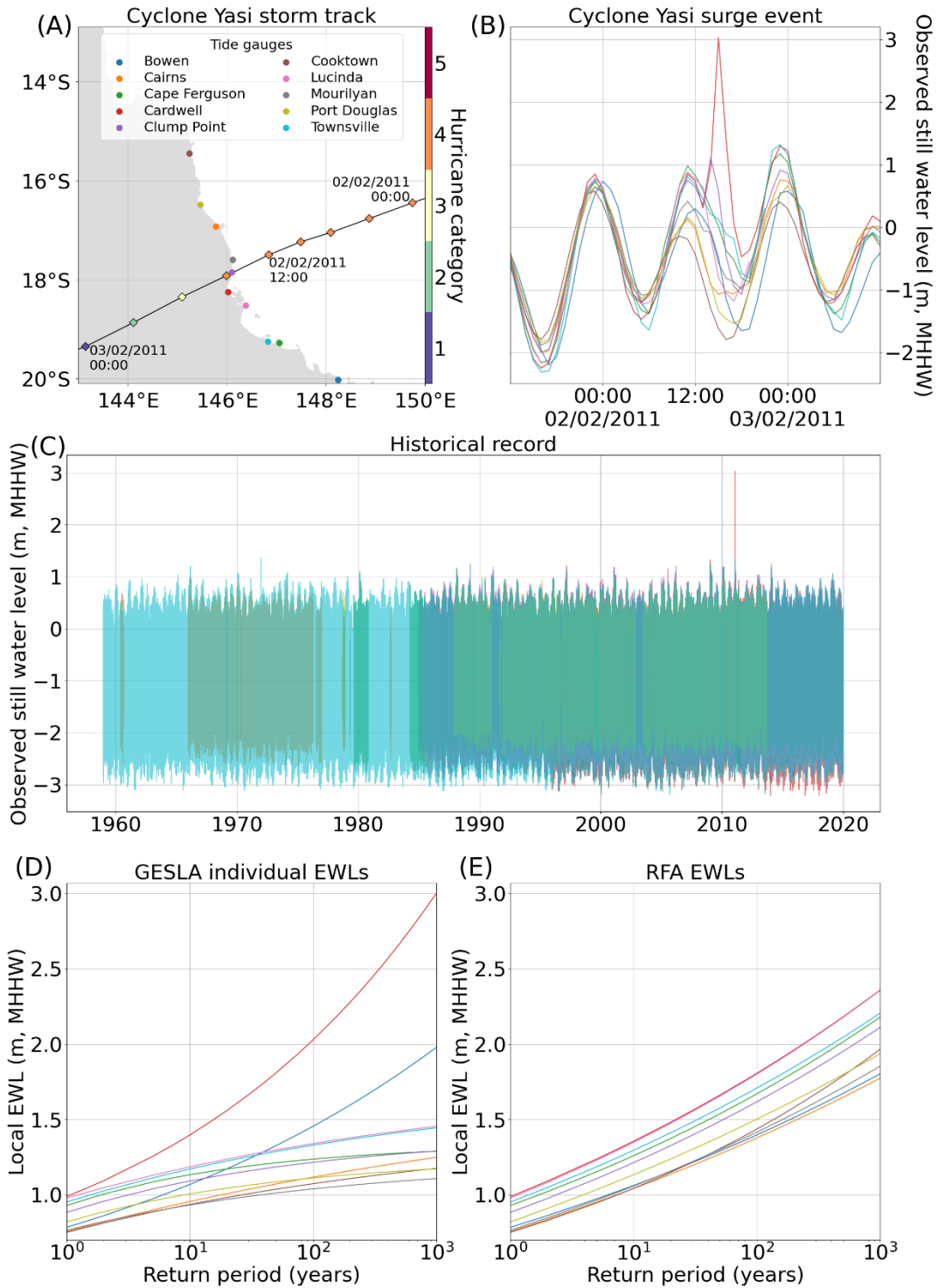
516

## 517 4.2 Tropical Cyclone Yasi

518 Our second study objective is to illustrate how the RFA methodology previously described  
519 can draw on few, rare events, to provide more realistic representation of low frequency ESL  
520 exceedance probabilities across a region, using the case study of cyclone Yasi which  
521 impacted the Australian coastline in 2011. Cyclone Yasi made landfall on the North-eastern  
522 coast of Australia, in the Queensland region, between 14:00 and 15:00 UTC on the 2nd of  
523 February 2011. It is the strongest cyclone to have impacted the region since 1918, with  
524 possible windspeeds of 285km/h and minimum record pressure centre of 929 hPa (Australia  
525 Bureau of Meteorology, 2011). When it made landfall, Yasi was a category 4 storm on the  
526 Saffir-Sampson scale. The path and strength of the storm are shown in Fig. 5A.

527 The total water levels, relative to mean higher high water, for all the tide gauges in the  
528 region are shown in Fig. 5B. Cardwell had the highest surge, and highest total water level, by  
529 a considerable margin compared to neighbouring tide gauges, receiving a surge of over 3m  
530 above mean higher high water. Clump Point also showed a definitive but less substantial  
531 surge signal, whereas the other gauges showed much smaller surge effects or even no surge  
532 at all. The historical water level records of all the gauges in the regions are included in Fig.  
533 5C. The tide gauges span different temporal ranges, and many have years which are  
534 incomplete. The longest record is at Townsville, which started in the late 1950s. Despite this  
535 record, the largest event is cyclone Yasi by over 1.5m (at Cardwell).

536 Based on this historical record, no other surge event of this magnitude has impacted this  
537 section of coastline since the records began. There are, however, records of other historic  
538 extreme events that predate tide gauges affecting the region. For example, Cyclone Mahina,  
539 which made landfall in Princess Charlotte Bay (approximately 100km north of Cooktown) in  
540 1899, reportedly had a surge height approaching 10m (Needham et al., 2015). The idea that  
541 this stretch of coastline is at risk of TC generated ESLs is further supported by STORM, a  
542 dataset of 10,000 years of synthetic hurricane tracks (Bloemendaal et al., 2020). IBTrACS  
543 shows just eight category 4 and 5 hurricanes impacting this 700km stretch of coastline  
544 between 1980 and 2022 (shown in the Appendix Fig. A2; (Knapp et al., 2010)). In contrast,  
545 the STORM dataset has 333 events affecting the area, producing a more continuous spread  
546 of landfall locations along the coastline. In addition, large surges are sometimes not  
547 captured in this region due to the lack of gauges in rural areas (Needham et al., 2015).



548

549 *Figure 5: Tropical Cyclone Yasi: (A) The storm track of cyclone Yasi, covering a 24-hour period over the landfall event. The*  
 550 *locations of the 10 closest tide gauges along the Queensland coast are also included. Times are in UTC. (B) The observed*  
 551 *water level timeseries for the same 24-hour period at each of the 10 tide gauges in the region. Times are in UTC. (C) The*  
 552 *entire historical record of all 10 gauges in the region. (D) The return period curves of individual gauges fit with Generalised*  
 553 *Pareto distribution. (E) The return period curves at the gauge locations from the RFA.*

554 The return period curves, calculated by fitting a Generalised Pareto distribution to the  
 555 peaks-over-threshold water levels at each individual tide gauge, for each of the 10 gauges in

556 the region, are shown in Fig. 5D. As expected, Cardwell has the largest return levels and the  
557 steepest curve. All the other gauges, except Bowen, exhibit negative shape parameters,  
558 characterised by a decreasing gradient of the return period curves. In a region which is  
559 prone to TCs, this is a dangerous underestimation of the risk from cyclone induced surges. In  
560 some coastal ESL studies, ESLs are calculated at each gauge, and then interpolated along the  
561 coastline, such as in the UK (Environment Agency, 2018). In this case, that approach would  
562 lead to a gross disparity from the actual risk of storm surges to coastal communities in the  
563 area.

564 In contrast, Fig. 5E shows the return period curves estimated from the RFA at the tide gauge  
565 locations. All of the curves now have positive shape parameters, characterised by increasing  
566 gradients of the curves. The curves of Cardwell and Bowen have been reduced somewhat,  
567 while all the other curves have been increased significantly. This demonstrates the  
568 regionalisation process, by which the extreme event at Cardwell can be used to propagate  
569 the risk along the coastline to areas which have not had an extreme event on record, or  
570 have short, incomplete, or non-existent tide gauge records. This reinforces the key strengths  
571 of the RFA, namely: (1) the ability to spatially account for rare extreme events, (2) the use of  
572 short and incomplete tide gauge records to produce robust parameter fits, and (3) the  
573 ability to downscale the results into regions which aren't covered by tide gauges at all.

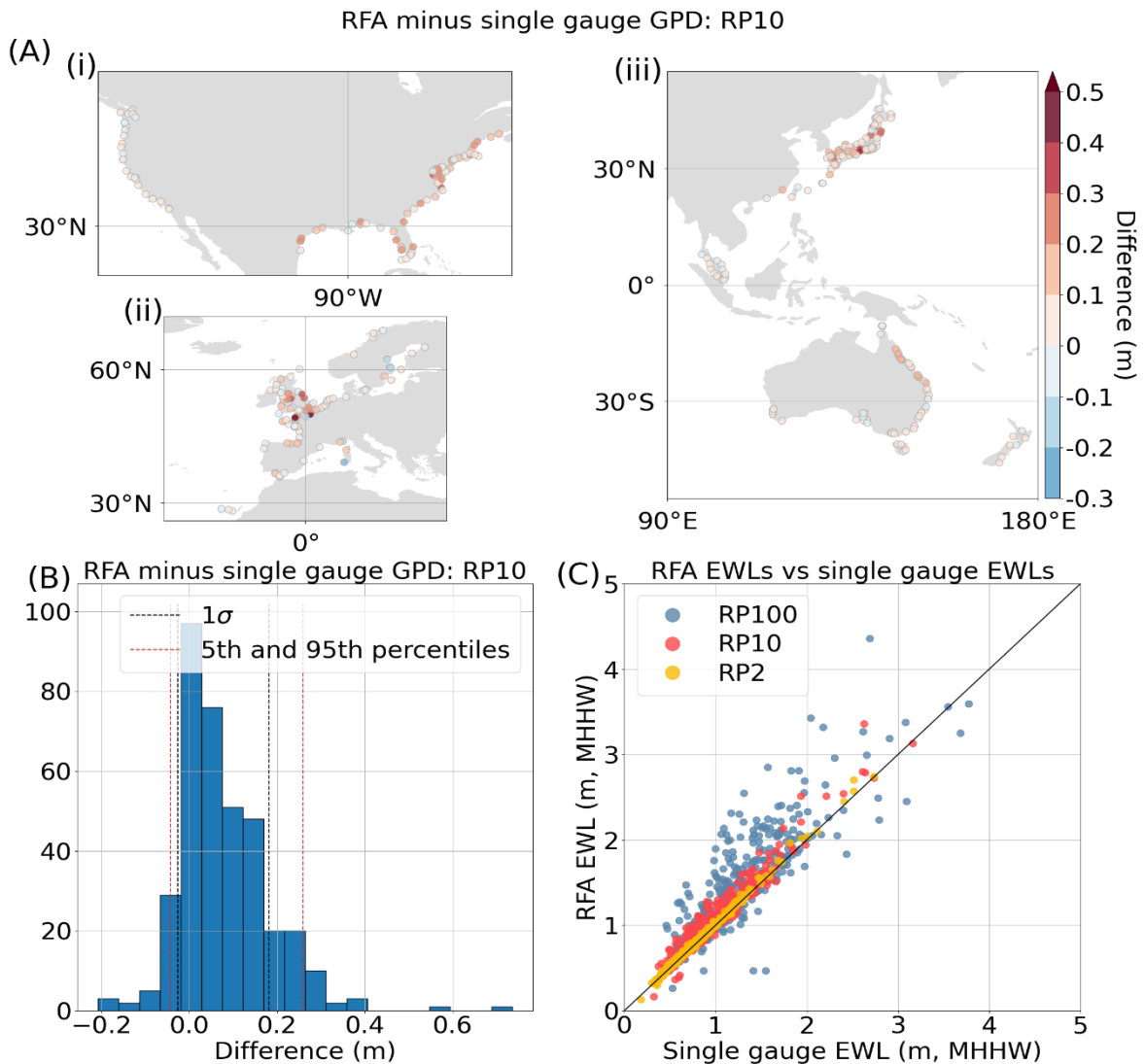
#### 574 4.3 Comparisons with GESLA

575 The third objective is to validate ESLs calculated using our RFA against those calculated  
576 directly from the measured GESLA-3 global tide gauge database. Contrasting the RFA results  
577 with ESL exceedance probabilities calculated through a Generalised Pareto distribution fit at  
578 individual tide gauges yields promising results. Fig. 6A shows the spatial distribution of the  
579 difference at the 1-in-10-year return period for Europe, the United States, and the East  
580 Pacific. In areas impacted by TCs (e.g., the Gulf of Mexico, North-Eastern Coast of Australia,  
581 and Japan) we broadly see that the RFA has increasing return levels across most gauges.  
582 Increases in the 1-in-10-year return level are also observed in areas usually associated with  
583 extra-tropical storms (e.g., Europe), suggesting gauges in these regions also suffer from  
584 under sampling of rare surge events. Extreme surge events can be undersampled for two  
585 reasons. Firstly, by their very nature, they are rare and might never have occurred at a



586 specific location. Secondly, as a result of a scarcity of in-situ tide gauges, surges can occur  
587 and remain unrecorded.

588 In all areas shown in Figure 6A, some gauges show decreases in the return levels. This could  
589 be driven by either shape parameter limiting (to prevent unrealistically large water levels),  
590 an anomalously large number of events impacting the gauge, or due to a single anomalously  
591 large event impacting the gauge, which is then smoothed out through the regionalisation  
592 process, as was the case in Cardwell, Australia (Fig. 5E). Of the gauges shown in the Fig. 6A,  
593 only 5 had limited shape parameters, which were located in the Gulf of Mexico. The  
594 distribution of the differences at RP10 is shown in Fig. 6B with a positive skew, detailing the  
595 5<sup>th</sup> and 95<sup>th</sup> percentiles as -8cm and 27cm respectively. The spread of the data increases  
596 across the three selected return periods (1-in-2, 1-in-10 and 1-in-100 year) presented in in  
597 Fig. 6C, as well as the mean bias, which increased from 2 cm in the 1-in-2 year return level,  
598 to 21cm in the 1-in-100 year return level.



599

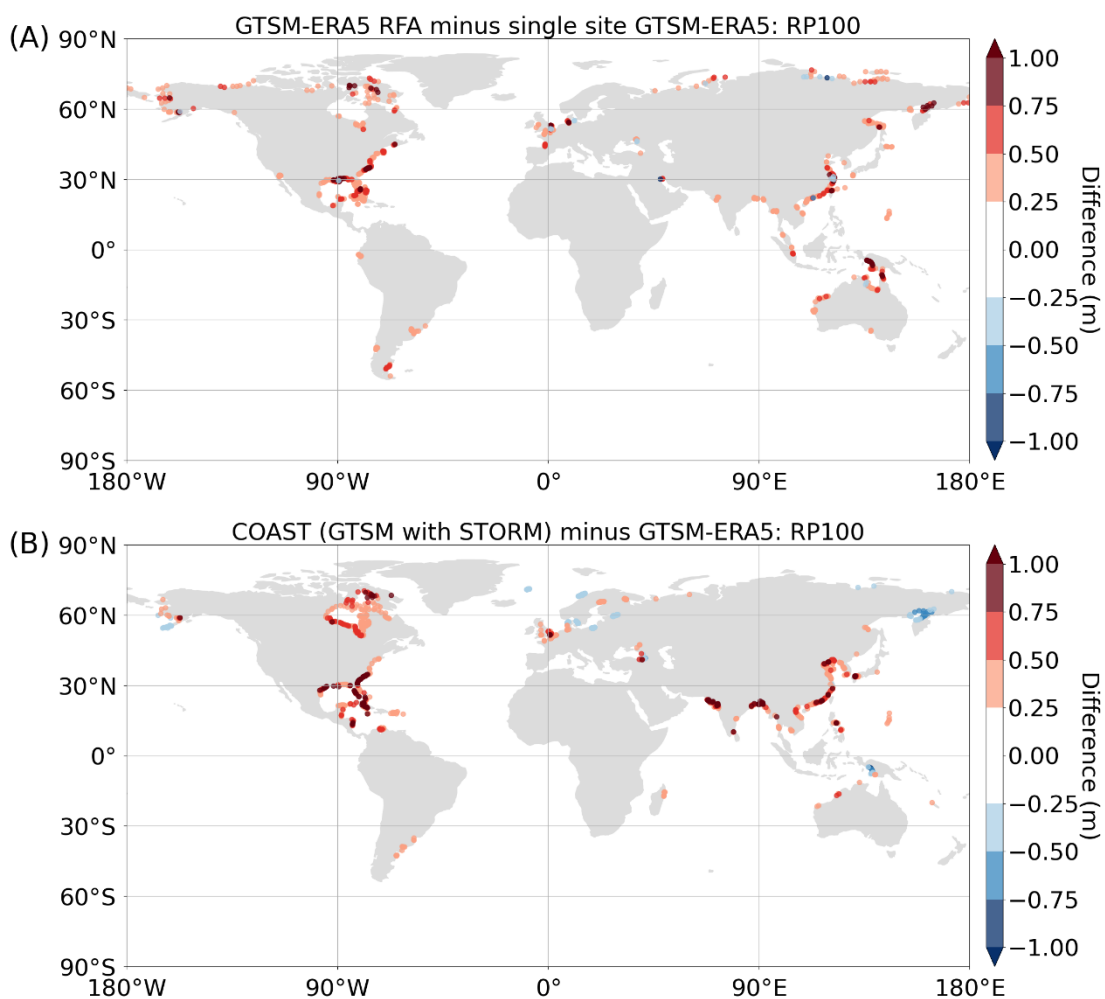
600 *Figure 6: Comparison of RFA water levels against extreme water levels calculated at individual gauges from GESLA by fitting*  
 601 *a Generalised Pareto distribution to peaks-over-threshold water levels. (A) The spatial distribution of the difference at RP10*  
 602 *for (i) the contiguous US, (ii) Europe, (iii) Japan, Malaysia, Australia and New Zealand, (B) a histogram of the distributions of*  
 603 *difference at RP10, including the locations of the 5<sup>th</sup> and 95<sup>th</sup> percentiles and 1 standard deviation from the mean, and (C) a*  
 604 *scatter plot of EWLs (RP2, RP10, RP100) from the RFA and the EWLs calculated using a single site Generalised Pareto*  
 605 *distribution fit. The black line indicates a 1:1 perfect fit.*

606

#### 607 4.4 Quantifying the increases made by the RFA when compared to single site 608 analysis

609 The fourth objective is to quantify the increases made to ESL exceedance probabilities in TC  
 610 prone areas by the RFA, when compared to a single site analysis. Figure 7A shows the  
 611 deviation in the 1-in-100-year return period between the GTSM-ERA5 RFA carried out across  
 612 the global coastline, and a single site peaks-over-threshold analysis of GTSM-ERA5 water  
 613 level records. Only differences greater or less than 0.25 m and -0.25 m respectively, are

614 plotted. There are evident increases to RFA ESLs in areas prone to TCs. The Gulf of Mexico,  
 615 the East Coast of the US, Southern China, and the North-East Coast of Australia show the  
 616 largest increases. Sporadic negative differences are also observed in Fig. 7A, which are  
 617 driven by a smoothing of ESL exceedance probabilities at locations which have experienced  
 618 anomalously high ESL compared to the local region. From this we see that the RFA is capable  
 619 of incorporating the influence of TCs that were not present in the historical record, but  
 620 statistically could occur as indicated by the regional characteristic.

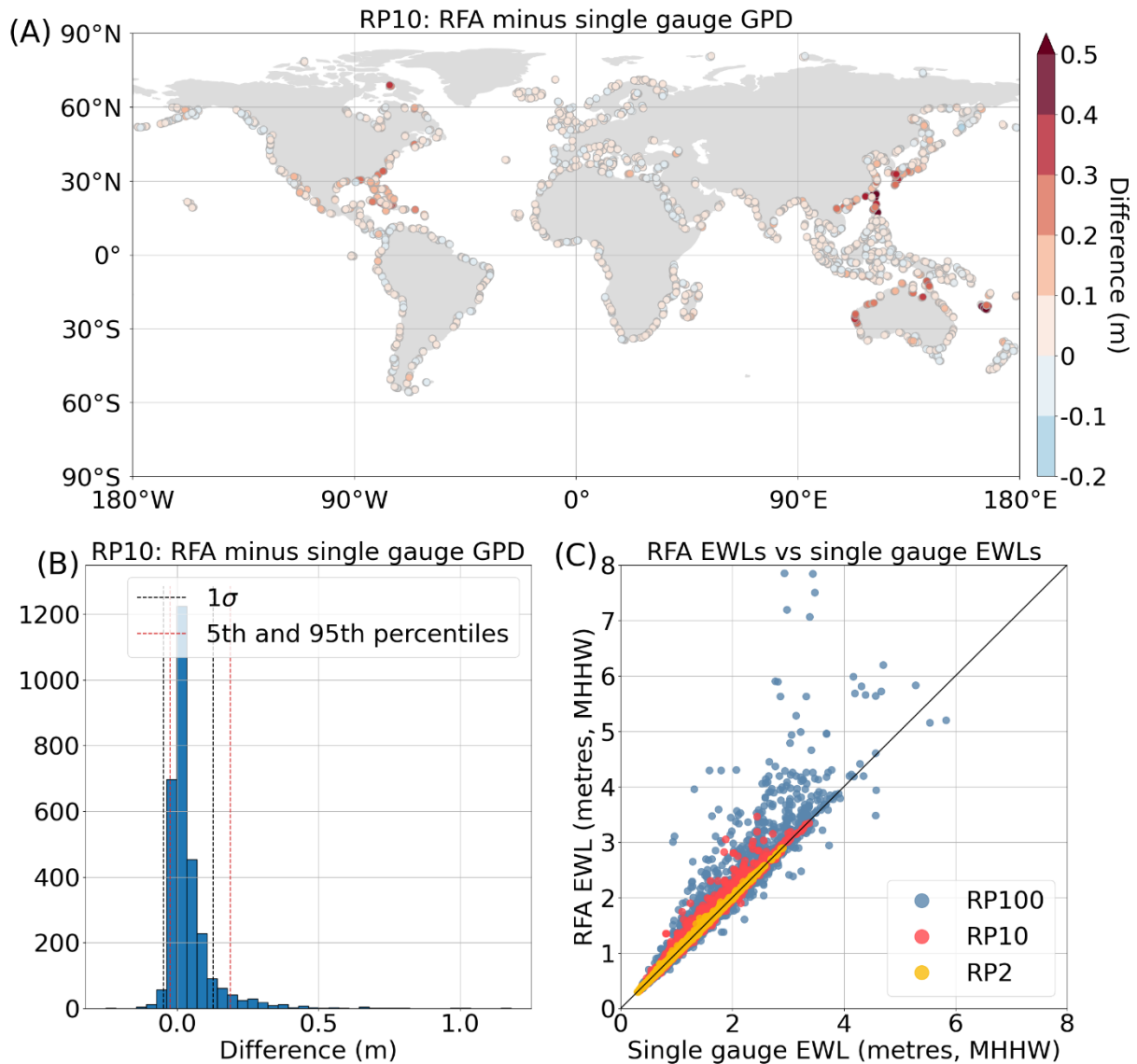


621

622 *Figure 7: The spatial distributions of: (A) the differences between the GTSM-ERA5 RFA 1-in-100-year return period (RP100)*  
 623 *and the RP100 of single site GTSM-ERA5 data fit with a Generalised Pareto distribution to the peaks-over-threshold water*  
 624 *levels; and (B) the differences in RP100 published by the COAST-RP (GTSM forced with STORM) paper (Dullaart et al., 2021)*  
 625 *and RP100 published by the original GTSM paper (Muis et al., 2020). Only differences greater or less than 0.25 m and -0.25*  
 626 *m, respectively, are plotted.*

627 These findings can be supported by the results shown in Fig. 7B, which shows the  
628 differences between COAST-RP and GTSM-ERA5. COAST-RP is GTSM forced with STORM  
629 (10,000 years of synthetic TCs) in areas prone to TC activity, instead of ERA5 (Dullaart et al.,  
630 2021). The areas of positive difference highlight locations where COAST-RP is greater than  
631 GTSM-ERA5, and so give an indication of the areas in which the synthetic hurricanes make  
632 landfall. These patterns are broadly similar to those of the RFA, shown in Fig. 7A. However,  
633 there are two areas which stand out for being poorly characterised by the RFA, namely: the  
634 Bay of Bengal and the western Gujarat region of India. Large differences are also observed  
635 in Hudson Bay, Canada, however we suspect these discrepancies are the result of  
636 differences in the approach to modelling extra-tropical regions, as TCs do not make landfall  
637 here.

638 Figure 8 shows the results of the leave-one-out cross validation of the global coastal LEWLs.  
639 In general, the RFA tends to increase return levels due to the regionalisation process. These  
640 findings match those of (Sweet et al., 2022, Sweet et al., 2020) upon which our approach is  
641 based. This is evident throughout the world, with the majority of gauges exhibiting increases  
642 of less than 5 cm at the 1-in-10-year return period (Fig. 8A). The central 90th percentile  
643 band of the data for the 1-in-10-year return period ranges from -3 to 18 cm, as shown in Fig.  
644 8B. However, the spread of the data is more pronounced at the higher return periods, as  
645 shown in Fig. 8C. Some regions of the world have greater increases, in the order of 30 – 40  
646 cm for the 1-in-10 year return period. These gauges are mostly concentrated in TC basins,  
647 namely the Caribbean, the Gulf of Mexico, Japan, China, the Philippines, plus the East and  
648 West Coasts of Australia. This demonstrates the process by which the RFA better represents  
649 extreme rare events that are typically under sampled in the historical record. By drawing on  
650 all the events captured by gauges across the region, the RFA reveals that there is greater risk  
651 of extreme events by considering their potential occurrence in areas that, by chance, have  
652 not been previously impacted as observed in historical records. Similarly, oversampling is  
653 clearly evident at 1-in-100-year return periods, for which nearly a third of locations show  
654 decreases in ESL exceedance probabilities compared to the single site analysis. The  
655 magnitude of these decreases tend to be much smaller than the increases seen.



656

657

658 *Figure 8: The results of the leave-one-out cross validation of the RFA on GTSM-ERA5 gauges. (A) The spatial distribution of*  
 659 *difference between the leave-one-out cross validation RFA RP10 (1 in 10-year return period) and the single site Generalised*  
 660 *Pareto distribution RP10, (B) a histogram of the distribution of the differences in RP10 including the locations of the 5th and*  
 661 *95th percentiles and 1 standard deviation from the mean, and (C) a scatter plot of EWLs (RP2, RP10, and RP100) predicted*  
 662 *using the leave-one-out cross validation RFA and the EWLs calculated using a single site Generalised Pareto fit.*  
 663 *The black line indicates a 1:1 perfect fit.*

## 664 5. Discussion

665 The ESL exceedance probabilities dataset that is presented in this paper is the first global  
 666 dataset, to our knowledge, to be derived using an RFA approach, using a synthesis of  
 667 observed and modelled hindcast data. The resulting data is output at high resolution (~1  
 668 km) along the entire global coastline (excluding Antarctica), includes wave setup, and better

669 captures the coastal flood risk from TCs. This approach is notable for being computationally  
670 inexpensive compared to more traditional approaches for deriving ESL exceedance  
671 probabilities via hydrodynamic modelling.

672 As previously discussed in the introduction section, relying solely on observational records  
673 to estimate ESL exceedance probabilities can significantly bias results. To fit robust  
674 parameter estimates and obtain confident exceedance probabilities sufficient for informing  
675 flood risk managers, long term and consistent high quality observational records are needed  
676 (Coles, 2001). While some tide gauge and wave records span numerous decades, many  
677 records only cover a handful of recent decades (e.g., 10-30 years) or have significant gaps in  
678 their historical records. This often means quality data is excluded from analyses as their  
679 records are too short to produce robust parameter estimates. Furthermore, gauges are  
680 relatively sparse, especially in less populated areas and developing nations. While surges  
681 and waves typically impact large regions, peak water levels are usually only observed over  
682 smaller areas (i.e., a single bay, estuary or beach). As a result, measured records can easily  
683 miss the maximum of an extreme event, thus mischaracterising extreme water levels of the  
684 event. As such, rare extreme events that characterise the upmost tails of the distributions of  
685 ESLs, such as TCs, are repeatedly under sampled in the historic record, in both frequency  
686 and magnitude.

687 By using an RFA approach, we demonstrate how we have improved these issues. The RFA  
688 can be viewed as a space-for-time approach, where long historical records (which give  
689 robust parameter estimates) are substituted for a collection of shorter records that cover a  
690 larger area. The volume of data (and subsequent extreme events) is retained, but the  
691 individual records can be much shorter. In this study, records as short as 10 years have been  
692 utilised. Furthermore, the regionalisation process works to overcome the issues with gauge  
693 density by disseminating the hazard presented by rare extreme events, as shown using the  
694 Cyclone Yasi example. From the 10 gauges in the region, the only record to have captured  
695 an historic extreme surge event of the magnitude observed during Cyclone Yasi was  
696 Cardwell, despite this section of coastline being at known risk to TC activity. A single site  
697 analysis of tide gauge data in this region would likely underpredict the real risk of ESLs  
698 generated by TCs in areas which haven't had a direct impact in the observational record. On

699 the other hand, the damping of the return levels in the RFA output at Cardwell and Bowen  
700 could mean an underprediction of the risk from surges in these locations.

701 Global hydrodynamic models that simulate tide and surge (e.g., GTSM) or waves have been  
702 developed to substitute observational records, especially in regions not covered by tide  
703 gauges. These models have been demonstrated to represent historic extreme events to a  
704 high degree of accuracy when forced using historical observational data pertaining to the  
705 event (Yang et al., 2020). However, using these models for the characterisation of  
706 exceedance probabilities is limited by the availability of long term high-quality global  
707 reanalysis data, that captures the full extent of meteorological extremes that drive large  
708 surge events. The RFA aims to address this by using a space-for-time approach, however it  
709 is still limited by the bounds of the GTSM-ERA5 data. As demonstrated in Fig. 7, the  
710 distribution of increases to local return levels made by the RFA broadly follows the same  
711 patterns globally as the differences between COAST-RP and GTSM-ERA5. As TC hazard is  
712 typically underrepresented due to short records, it can be inferred that the increases  
713 observed across these regions are an improvement on a single site analysis.

714 While the RFA is capable of identifying areas of increased risk from TC activity, it is still  
715 constrained by the training data available. This is demonstrated in Fig. 7. Two distinct areas  
716 lack increased water levels in the RFA difference plot (Fig. 7A), namely: the Bay of Bengal  
717 and Northwestern coasts of India and Pakistan. ERA5, the forcing data used for GTSM-ERA5  
718 has been found to consistently underestimate TC intensity in both minimum sea level  
719 pressure and maximum windspeed (Dulac et al., 2023). Consequently, the intensity of  
720 extreme events in GTSM-ERA5 in these regions could underrepresent the potential hazard  
721 from TC activity. If the maximums of extremes are not captured in the reanalysis data, then  
722 the full magnitude of the surge cannot be simulated by GTSM-ERA5. As such, the RFA will  
723 have smaller or fewer extremes with which to draw data from when characterising rare  
724 extreme events, therefore leading to a persistent underestimation of the return levels.

725 Coastal flood hazard mapping is usually carried out using inundation models that simulate  
726 the propagation of water over the coastal floodplain. To accurately capture the footprint of  
727 the surge on the land, inundation models require high-resolution boundary conditions at  
728 regular intervals along the coastline. The density of boundary condition points needs to be  
729 sufficient to capture local variability in ESLs along a coastline, which can be caused by

730 bathymetric and topographic features such as narrow channels, enclosed bays, barrier  
731 island and estuaries. The spatial resolution of tide gauges, even in the areas of highest gauge  
732 density, is insufficient for direct use in inundation modelling and therefore requires some  
733 form of interpolation and/or extrapolation. Similarly, while GTSM-ERA5, is run at a  
734 reasonably high coastal resolution, publicly available data is only output at approximately  
735 50km resolution outside of Europe, and therefore does not meet the standards necessary  
736 for coastal floodplain inundation modelling. Using the RFA to downscale the regional  
737 extreme water levels allows for the possibility of implementing tide gauge data and the  
738 outputs from GTSM-ERA5 as boundary conditions for subsequent inundation models. In  
739 addition, the downscaling process involves scaling the water levels by tidal range and thus  
740 enables dynamic characteristics of the surge, such as amplification at the head of estuaries,  
741 to be reproduced in the inundation models. This downscaling process is, however, limited  
742 by the resolution of the tide model used to obtain the tidal range values. In the case of this  
743 study, FES2014 is output at 1/16<sup>th</sup> of a degree (approximately 7km at the equator).

744 Ultimately, the future of delineating the flood hazard from TCs lies in multi-ensemble  
745 models using 100's of 1,000's of years' worth of synthetically generated storms forcing high-  
746 resolution tide-surge-wave models. However, the computational cost of running such  
747 simulations is enormous when compared to the cost of running an RFA on a relatively short  
748 hindcast record. In the same way, dynamically modelled waves are usually excluded from  
749 global simulations that consider exceedance probabilities due to the computational  
750 expense. At the same time, failing to consider the joint dependence of surge and waves can  
751 lead to an underestimation of ESL exceedance levels by up to a factor of two along 30% of  
752 the global coastline (Marcos et al., 2019). This reinforces the significance of the RFA  
753 methodology in characterising global coastal flood risk.

754 Validating the RFA is nuanced, as assessing metrics compared with observed record is: (a)  
755 validating against the data used to build the RFA in the first place; and (b) not recognising  
756 the inadequacies of the tide gauge records that the RFA is attempting to mitigate. Leave-  
757 one-out cross validation highlights the strengths of the RFA, without succumbing to the  
758 shortfalls inherent in the observational record. The increased LEWLs in the regions prone to  
759 TC activity once again demonstrates the RFA's ability to spatially disperse the hazard of low  
760 probability extreme events across a region. It is worth noting that the leave-one-out cross



761 validation is the best possible representation of the RFA as only grid cells that use data from  
762 10 record locations are used, so each model is trained on the maximum amount of data  
763 possible. In some areas, the number of records used can be as low as three, and so the  
764 ability for the RFA to reproduce water levels in these regions could be compromised.

765 Applying the RFA as done in this study does have its limitations. Firstly, changing our  
766 definition of a homogeneous region would likely have a great impact on our results. In  
767 future iterations of this study, we recommend carrying out a sensitivity analysis to  
768 understand how using different maximum radii to select water level records impacts upon  
769 estimated extreme water levels within the region. Secondly, delineating the global coastline  
770 into 1° by 1° tiles and evaluating a different RFA for each tile results in some complex areas  
771 of coastline being summarised by a single regional growth function. Examples of this are  
772 seen in Japan, where exposed coastlines of the North Coast are contained in the same tile as  
773 a sheltered bay that is open to the South Coast. A solution to this would be to classify  
774 coastlines based on descriptors, as carried out by Sweet et al. (2020). These descriptors  
775 could include characteristics such as dominant forcing type, geographic location, and/or  
776 local coastal dynamics. The method used to incorporate wave setup is another constraint, as  
777 it has been greatly simplified for ease of global application. Improving upon this should also  
778 be a focus of future studies. Lastly, another limitation of the approach used in this study is  
779 the static shape parameter limiter. It is probable that the maximum shape parameter varies  
780 by location around the world, and that by implementing a fixed threshold globally we are  
781 perhaps limiting some of the most extreme events in some regions. Improving this section  
782 of the methodology is a high priority for future updates.

783 The outputs from the RFA should be supplemented with local knowledge wherever possible,  
784 and the uncertainties in the results should be considered before the data is used. The RFA is  
785 a powerful tool for estimating return levels in ungauged locations or in locations where the  
786 historical records are short or incomplete, but there are risks associated with both  
787 overpredicting and underpredicting surge heights. Underprediction can lead to complacency  
788 among coastal managers and the potentially dangerous assumption that communities are  
789 safe from surge risk. Conversely, overprediction can result in unnecessary cost for risk  
790 mitigation measures and potential economic loss driven by a lack of investment in a region  
791 deemed at risk. Disseminating the risk of TC generated surges over a region could lead to

792 overprediction in some locations, and so conducting sensitivity analyses to understand the  
793 robustness of findings is recommended, especially in the context of coastal management  
794 and safety assessments. The RFA has been developed in this study as a method for regional  
795 to continental to global scale risk analyses from globally available data, and not local  
796 studies. The results give a first order approximation of extreme water levels in ungauged  
797 locations. It is not expected that they would be used in the design for local flood defences,  
798 for example.

799 Going forward, the RFA framework developed in this study can be easily updated with the  
800 availability of new data. Possible next steps could also include using GTSM simulations of  
801 future climate scenarios, as well as measured wave data. To this end, a global wave dataset  
802 similar to GESLA would be instrumental in collating wave data from the numerous buoys  
803 globally. Future updates could also include an assessment of using different extreme value  
804 distributions, perhaps following the mixed climate approach of (O’Grady et al., 2022).

805 In the near future, we plan to use the global exceedance probabilities derived in this paper  
806 as boundary conditions for inundation modelling of the coastal floodplain of the entire  
807 globe, using the 2D hydraulic model LISFLOOD-FP (Bates et al., 2010). This presents an  
808 exciting opportunity to provide an invaluable resource that will help to better quantify  
809 global coastal flood risk.

810

## 811 6. Conclusions

812 In this paper we have demonstrated an RFA approach utilising both measured and modelled  
813 hindcast records to estimate ESL exceedance probabilities, including wave setup, at high  
814 resolution (~1 km) along the entire global coastline (with the exception of Antarctica). Our  
815 methodology is computationally inexpensive and is more effective in accurately estimating  
816 the low frequency exceedance probabilities that are associated with rare extreme events,  
817 compared to approaches that consider data from single sites. We have demonstrated, using  
818 Cyclone Yasi (2011) which impacted the Australia coast, the ability of the RFA to better  
819 characterise ESLs in regions prone to TC activity. Furthermore, on the global scale we have  
820 exemplified how the RFA, when trained on relatively short reanalysis data, can reproduce  
821 patterns of increased water levels similar to those present in dynamic simulations of 10,000

822 years of synthetic hurricane tracks. The RFA methodology shown provides a promising  
823 avenue for improving our understanding of coastal flooding and enhancing our ability to  
824 prepare for and mitigate its devastating impacts. In the future, we plan to use the  
825 exceedance probabilities from this study as boundary conditions for an inundation model  
826 covering the global coastal floodplain.

827

## 828 7. References

829

830 Amadeo, K.: Hurricane Harvey Facts, Damage and Costs, 1–5 pp., 2019.

831 Andrée, E., Su, J., Larsen, M. A. D., Madsen, K. S., and Drews, M.: Simulating major storm surge  
832 events in a complex coastal region, *Ocean Modelling*, 162,  
833 <https://doi.org/10.1016/j.ocemod.2021.101802>, 2021.

834 Andreevsky, M., Hamdi, Y., Griolet, S., Bernardara, P., and Frau, R.: Regional frequency analysis of  
835 extreme storm surges using the extremogram approach, *Natural Hazards and Earth System Sciences*,  
836 20, <https://doi.org/10.5194/nhess-20-1705-2020>, 2020.

837 Arns, A., Wahl, T., Haigh, I. D., and Jensen, J.: Determining return water levels at ungauged coastal  
838 sites: a case study for northern Germany, *Ocean Dynamics*, 65, [https://doi.org/10.1007/s10236-015-](https://doi.org/10.1007/s10236-015-0814-1)  
839 0814-1, 2015.

840 Australia Bureau of Meteorology: Severe Tropical Cyclone Yasi, 2011.

841 Bardet, L., Duluc, C. M., Rebour, V., and L’Her, J.: Regional frequency analysis of extreme storm  
842 surges along the French coast, *Natural Hazards and Earth System Science*, 11,  
843 <https://doi.org/10.5194/nhess-11-1627-2011>, 2011.

844 Barnard, P. L., Erikson, L. H., Foxgrover, A. C., Hart, J. A. F., Limber, P., O’Neill, A. C., van Ormondt,  
845 M., Vitousek, S., Wood, N., Hayden, M. K., and Jones, J. M.: Dynamic flood modeling essential to  
846 assess the coastal impacts of climate change, *Scientific Reports*, 9, [https://doi.org/10.1038/s41598-](https://doi.org/10.1038/s41598-019-40742-z)  
847 019-40742-z, 2019.

848 Bates, P. D., Horritt, M. S., and Fewtrell, T. J.: A simple inertial formulation of the shallow water  
849 equations for efficient two-dimensional flood inundation modelling, *Journal of Hydrology*, 387,  
850 <https://doi.org/10.1016/j.jhydrol.2010.03.027>, 2010.

851 Bates, P. D., Quinn, N., Sampson, C., Smith, A., Wing, O., Sosa, J., Savage, J., Olcese, G., Neal, J.,  
852 Schumann, G., Giustarini, L., Coxon, G., Porter, J. R., Amodeo, M. F., Chu, Z., Lewis-Gruss, S.,  
853 Freeman, N. B., Houser, T., Delgado, M., Hamidi, A., Bolliger, I., E. McCusker, K., Emanuel, K.,  
854 Ferreira, C. M., Khalid, A., Haigh, I. D., Couasnon, A., E. Kopp, R., Hsiang, S., and Krajewski, W. F.:  
855 Combined Modeling of US Fluvial, Pluvial, and Coastal Flood Hazard Under Current and Future  
856 Climates, *Water Resources Research*, 57, <https://doi.org/10.1029/2020WR028673>, 2021.

857 Bingham, R. J. and Haines, K.: Mean dynamic topography: Intercomparisons and errors, *Philosophical*  
858 *Transactions of the Royal Society A: Mathematical, Physical and Engineering Sciences*, 364,  
859 <https://doi.org/10.1098/rsta.2006.1745>, 2006.

860 Bloemendaal, N., Haigh, I. D., de Moel, H., Muis, S., Haarsma, R. J., and Aerts, J. C. J. H.: Generation  
861 of a global synthetic tropical cyclone hazard dataset using STORM, *Scientific Data*, 7,  
862 <https://doi.org/10.1038/s41597-020-0381-2>, 2020.

863 Calafat, F. M., Wahl, T., Tadesse, M. G., and Sparrow, S. N.: Trends in Europe storm surge extremes  
864 match the rate of sea-level rise, *Nature*, 603, <https://doi.org/10.1038/s41586-022-04426-5>, 2022.

865 Caldwell, P. C., Merrifield, M. A., and Thompson, P. R.: Sea level measured by tide gauges from global  
866 oceans — the Joint Archive for Sea Level holdings (NCEI Accession 0019568), Version 5.5, NOAA  
867 National Centers for Environmental Information, 2015.

868 Campos, R. M., Guedes Soares, C., Alves, J. H. G. M., Parente, C. E., and Guimaraes, L. G.: Regional  
869 long-term extreme wave analysis using hindcast data from the South Atlantic Ocean, *Ocean*  
870 *Engineering*, 179, <https://doi.org/10.1016/j.oceaneng.2019.03.023>, 2019.

871 Coles, S.: *An Introduction to Statistical Modeling of Extreme Values*, Springer, Bristol, 1–221 pp.,  
872 2001.

873 Dean, R. and Walton, T.: Wave Setup, in: *Handbook of Coastal and Ocean Engineering*, vol. 1–2,  
874 World Scientific Publishing co., 1–24, <https://doi.org/10.1142/10353>, 2010.

875 Dulac, W., Cattiaux, J., Chauvin, F., Bourdin, S., and Fromang, S.: Assessing the representation of  
876 tropical cyclones in ERA5 with the CNRM tracker, *Climate Dynamics*,  
877 <https://doi.org/10.1007/s00382-023-06902-8>, 2023.

878 Dullaart, J. C. M., Muis, S., Bloemendaal, N., Chertova, M. V., Couasnon, A., and Aerts, J. C. J. H.:  
879 Accounting for tropical cyclones more than doubles the global population exposed to low-probability  
880 coastal flooding, *Communications Earth and Environment*, 2, [https://doi.org/10.1038/s43247-021-](https://doi.org/10.1038/s43247-021-00204-9)  
881 [00204-9](https://doi.org/10.1038/s43247-021-00204-9), 2021.

882 Environment Agency: *Coastal flood boundary conditions for the UK: 2018 update*, 116 pp., 2018.

883 European Space Agency: *Copernicus Global Digital Elevation Model, Open Topology*, 1,  
884 <https://doi.org/doi.org/10.5069/G9028PQB>, 2021.

885 Fanti, V., Ferreira, Ó., Kümmerer, V., and Loureiro, C.: Improved estimates of extreme wave  
886 conditions in coastal areas from calibrated global reanalyses, *Communications Earth and*  
887 *Environment*, 4, <https://doi.org/10.1038/s43247-023-00819-0>, 2023.

888 Frau, R., Andreewsky, M., and Bernardara, P.: The use of historical information for regional  
889 frequency analysis of extreme skew surge, *Natural Hazards and Earth System Sciences*, 18,  
890 <https://doi.org/10.5194/nhess-18-949-2018>, 2018.

891 Haigh, I. D., MacPherson, L. R., Mason, M. S., Wijeratne, E. M. S., Pattiaratchi, C. B., Crompton, R. P.,  
892 and George, S.: Estimating present day extreme water level exceedance probabilities around the  
893 coastline of Australia: Tropical cyclone-induced storm surges, *Climate Dynamics*, 42,  
894 <https://doi.org/10.1007/s00382-012-1653-0>, 2014.

895 Haigh, I. D., Wadey, M. P., Wahl, T., Ozsoy, O., Nicholls, R. J., Brown, J. M., Horsburgh, K., and  
896 Gouldby, B.: Spatial and temporal analysis of extreme sea level and storm surge events around the  
897 coastline of the UK, <https://doi.org/10.1038/sdata.2016.107>, 2016.

898 Haigh, I. D., Marcos, M., Talke, S. A., Woodworth, P. L., Hunter, J. R., Hague, B. S., Bradshaw, E., and  
899 Thompson, P.: *GESLA Version 3: A major update to the global higher-frequency sea-level dataset*,  
900 *EarthArXiv*, 1–34, 2021.

901 Hall, J. A., Gill, S., Obeysekera, J., Sweet, W., Knuuti, K., and Marburger, J.: *Regional Sea Level*  
902 *Scenarios for Coastal Risk Management: Managing the Uncertainty of Future Sea Level Change and*  
903 *Extreme Water Levels for Department of Defense Coastal Sites Worldwide*, 224, 2016.

904 Hamdi, Y., Duluc, C. M., Bardet, L., and Rebour, V.: Use of the spatial extremogram to form a  
905 homogeneous region centered on a target site for the regional frequency analysis of extreme storm  
906 surges, *International Journal of Safety and Security Engineering*, 6, [https://doi.org/10.2495/SAFE-V6-](https://doi.org/10.2495/SAFE-V6-N4-777-781)  
907 [N4-777-781](https://doi.org/10.2495/SAFE-V6-N4-777-781), 2016.

908 Hersbach, H., Bell, B., Berrisford, P., Hirahara, S., Horányi, A., Muñoz-Sabater, J., Nicolas, J., Peubey,  
909 C., Radu, R., Schepers, D., Simmons, A., Soci, C., Abdalla, S., Abellan, X., Balsamo, G., Bechtold, P.,  
910 Biavati, G., Bidlot, J., Bonavita, M., De Chiara, G., Dahlgren, P., Dee, D., Diamantakis, M., Dragani, R.,  
911 Flemming, J., Forbes, R., Fuentes, M., Geer, A., Haimberger, L., Healy, S., Hogan, R. J., Hólm, E.,  
912 Janisková, M., Keeley, S., Laloyaux, P., Lopez, P., Lupu, C., Radnoti, G., de Rosnay, P., Rozum, I.,  
913 Vamborg, F., Villaume, S., and Thépaut, J.-N.: The ERA5 global reanalysis, *Quarterly Journal of the*  
914 *Royal Meteorological Society*, 146, 1999–2049, <https://doi.org/https://doi.org/10.1002/qj.3803>,  
915 2020.

916 Hosking, J. R. M. and Wallis, J. R.: *Regional Frequency Analysis: An approach based on L-moments*,  
917 Cambridge University Press, New York., Cambridge Universtiy Press, 238 pp.,  
918 <https://doi.org/https://doi.org/10.1017/CBO9780511529443>, 1997.

919 India Meteorological Department: *Super Cyclonic Storm Amphan over the southeast Bay of Bengal:*  
920 *Summary*, 1–57 pp., 2020.

921 Irish, J. L., Resio, D. T., and Ratcliff, J. J.: The influence of storm size on hurricane surge, *Journal of*  
922 *Physical Oceanography*, 38, <https://doi.org/10.1175/2008JPO3727.1>, 2008.

923 James, G., Witten, D., Hastie, T., and Tibshirani, R.: *An Introduction to Statistical Learning*, Springer,  
924 441 pp., <https://doi.org/10.1007/9781461471387>, 2013.

925 Knapp, K. R., Kruk, M. C., Levinson, D. H., Diamond, H. J., and Neumann, C. J.: The international best  
926 track archive for climate stewardship (IBTrACS), *Bulletin of the American Meteorological Society*, 91,  
927 <https://doi.org/10.1175/2009BAMS2755.1>, 2010.

928 Kumar, S., Lal, P., and Kumar, A.: Influence of Super Cyclone “Amphan” in the Indian Subcontinent  
929 amid COVID-19 Pandemic, *Remote Sensing in Earth Systems Sciences*, 4,  
930 <https://doi.org/10.1007/s41976-021-00048-z>, 2021.

931 Liang, B., Gao, H., and Shao, Z.: Characteristics of global waves based on the third-generation wave  
932 model SWAN, *Marine Structures*, 64, <https://doi.org/10.1016/j.marstruc.2018.10.011>, 2019.

933 Lucas, C., Muraleedharan, G., and Guedes Soares, C.: Regional frequency analysis of extreme waves  
934 in a coastal area, *Coastal Engineering*, 126, <https://doi.org/10.1016/j.coastaleng.2017.06.002>, 2017.

935 Lyard, F. H., Allain, D. J., Cancet, M., Carrère, L., and Picot, N.: FES2014 global ocean tide atlas:  
936 Design and performance, *Ocean Science*, 17, 615–649, <https://doi.org/10.5194/os-17-615-2021>,  
937 2021.

938 Marcos, M., Rohmer, J., Vousedoukas, M. I., Mentaschi, L., Le Cozannet, G., and Amores, A.: Increased  
939 Extreme Coastal Water Levels Due to the Combined Action of Storm Surges and Wind Waves,  
940 *Geophysical Research Letters*, 46, <https://doi.org/10.1029/2019GL082599>, 2019.

941 McGranahan, G., Balk, D., and Anderson, B.: The rising tide: Assessing the risks of climate change and  
942 human settlements in low elevation coastal zones, *Environment and Urbanization*, 19,  
943 <https://doi.org/10.1177/0956247807076960>, 2007.

944 Mitchell, D., Hawker, L., Savage, J., Bingham, R., Lord, N. S., Khan, M. J. U., Bates, P., Durand, F.,  
945 Hassan, A., Huq, S., Islam, A. S., Krien, Y., Neal, J., Sampson, C., Smith, A., and Testut, L.: Increased  
946 population exposure to Amphan-scale cyclones under future climates, *Climate Resilience and*  
947 *Sustainability*, 1, 1–16, <https://doi.org/10.1002/cli.2.36>, 2022.

948 Mori, N., Yasuda, T., Arikawa, T., Kataoka, T., Nakajo, S., Suzuki, K., Yamanaka, Y., Webb, A.,  
949 Takahashi, T., Kim, S., Araki, S., Shibutani, Y., Yamano, T., Sakai, D., Takagawa, T., Tsuruta, N.,  
950 Kawaguchi, S., Asahi, S., Fujiki, T., Iwamoto, T., Chida, Y., Shibayama, T., Esteban, M., Takabatake, T.,  
951 Nakamura, R., Uno, K., Kakinoki, T., Nihei, Y., Inazu, D., Shigematsu, T., Sameshima, K., Honda, K.,  
952 Satomura, D., Tsujisawa, I., Kumagai, K., Sugahara, N., Emoto, S., and Tajima, Y.: 2018 Typhoon Jebi  
953 post-event survey of coastal damage in the Kansai region, Japan, *Coastal Engineering Journal*, 61,  
954 <https://doi.org/10.1080/21664250.2019.1619253>, 2019.

955 Muis, S., Verlaan, M., Winsemius, H. C., Aerts, J. C. J. H., and Ward, P. J.: A global reanalysis of storm  
956 surges and extreme sea levels, *Nature Communications*, 7, 11969,  
957 <https://doi.org/10.1038/ncomms11969>, 2016.

958 Muis, S., Apecechea, M. I., Dullaart, J., de Lima Rego, J., Madsen, K. S., Su, J., Yan, K., and Verlaan, M.:  
959 A High-Resolution Global Dataset of Extreme Sea Levels, Tides, and Storm Surges, Including Future  
960 Projections, *Frontiers in Marine Science*, 7, 1–15, <https://doi.org/10.3389/fmars.2020.00263>, 2020.

961 Mulet, S., Rio, M. H., Etienne, H., Artana, C., Cancet, M., Dibarboure, G., Feng, H., Husson, R., Picot,  
962 N., Provost, C., and Strub, P. T.: The new CNES-CLS18 global mean dynamic topography, *Ocean  
963 Science*, 17, 789–808, <https://doi.org/10.5194/os-17-789-2021>, 2021.

964 Needham, H. F., Keim, B. D., and Sathiaraj, D.: A review of tropical cyclone-generated storm surges:  
965 Global data sources, observations, and impacts, *Reviews of Geophysics*, 53, 545–591,  
966 <https://doi.org/10.1002/2014RG000477>, 2015.

967 Neumann, B., Vafeidis, A. T., Zimmermann, J., and Nicholls, R. J.: Future coastal population growth  
968 and exposure to sea-level rise and coastal flooding - A global assessment, *PLoS ONE*, 10,  
969 <https://doi.org/10.1371/journal.pone.0118571>, 2015.

970 Nicholls, R. J., Lincke, D., Hinkel, J., Brown, S., Vafeidis, A. T., Meyssignac, B., Hanson, S. E., Merkens,  
971 J. L., and Fang, J.: A global analysis of subsidence, relative sea-level change and coastal flood  
972 exposure, *Nature Climate Change*, 11, <https://doi.org/10.1038/s41558-021-00993-z>, 2021.

973 O’Grady, J. G., Stephenson, A. G., and McInnes, K. L.: Gauging mixed climate extreme value  
974 distributions in tropical cyclone regions, *Scientific Reports*, 12, <https://doi.org/10.1038/s41598-022-08382-y>, 2022.

976 Ramakrishnan, R., Remya, P. G., Mandal, A., Mohanty, P., Arayakandy, P., Mahendra, R. S., and Nair,  
977 T. M. B.: Wave induced coastal flooding along the southwest coast of India during tropical cyclone  
978 Tauktae, *Scientific Reports*, 12, <https://doi.org/10.1038/s41598-022-24557-z>, 2022.

979 Shaji, C., Kar, S. K., and Vishal, T.: Storm surge studies in the North Indian Ocean: A review, *Indian  
980 Journal of Marine Sciences*, 43, 2014.

981 Siah Sarani, A., Karami Khaniki, A., Aliakbari Bidokhti, A. A., and Azadi, M.: Numerical Modeling of  
982 Tropical Cyclone-Induced Storm Surge in the Gulf of Oman Using a Storm Surge–Wave–Tide Coupled  
983 Model, *Ocean Science Journal*, 56, <https://doi.org/10.1007/s12601-021-00027-x>, 2021.

984 Slocum, C. J., Razin, M. N., Knaff, J. A., and Stow, J. P.: Does ERA5 mark a new era for resolving the  
985 tropical cyclone environment?, *Journal of Climate*, 1–39, <https://doi.org/10.1175/jcli-d-22-0127.1>,  
986 2022.

987 Sweet, W. V., Genz, A. S., Obeysekera, J., and Marra, J. J.: A Regional Frequency Analysis of Tide  
988 Gauges to Assess Pacific Coast Flood Risk, 2020.

989 Sweet, W. V., Hamlington, B. D., Kopp, R. E., Weaver, C. P., Barnard, P. L., Bekaert, D., Brooks, W.,  
990 Craghan, M., Dusek, G., Frederikse, T., Garner, G., Genz, A. S., Krasting, J. P., Larour, E., Marcy, D.,  
991 Marra, J. J., Obeysekera, J., Osler, M., Pendleton, M., Roman, D., Schmied, L., Veatch, W., White, K.  
992 D., and Zuzak, C.: Global and Regional Sea Level Rise Scenarios for the United States, NOAA Technical  
993 Report NOS 01, 111 pp, 2022.

994 Taherkhani, M., Vitousek, S., Barnard, P. L., Frazer, N., Anderson, T. R., and Fletcher, C. H.: Sea-level  
995 rise exponentially increases coastal flood frequency, *Scientific Reports*, 10,  
996 <https://doi.org/10.1038/s41598-020-62188-4>, 2020.

997 Tanim, A. H. and Akter, A.: Storm-surge modelling for cyclone Mora in the northern Bay of Bengal,  
998 *Proceedings of the Institution of Civil Engineers: Maritime Engineering*, 172,  
999 <https://doi.org/10.1680/jmaen.2019.1>, 2019.

1000 Timmermans, B. W., Gommenginger, C. P., Dodet, G., and Bidlot, J. R.: Global Wave Height Trends  
1001 and Variability from New Multimission Satellite Altimeter Products, Reanalyses, and Wave Buoys,  
1002 *Geophysical Research Letters*, 47, <https://doi.org/10.1029/2019GL086880>, 2020.

1003 Vanem, E.: A regional extreme value analysis of ocean waves in a changing climate, *Ocean  
1004 Engineering*, 144, <https://doi.org/10.1016/j.oceaneng.2017.08.027>, 2017.

1005 Vousdoukas, M. I., Voukouvalas, E., Mentaschi, L., Dottori, F., Giardino, A., Bouziotas, D., Bianchi, A.,  
1006 Salamon, P., and Feyen, L.: Developments in large-scale coastal flood hazard mapping, *Natural  
1007 Hazards and Earth System Sciences*, 16, <https://doi.org/10.5194/nhess-16-1841-2016>, 2016.

1008 Wang, J. and Wang, Y.: Evaluation of the ERA5 Significant Wave Height against NDBC Buoy Data from  
1009 1979 to 2019, *Marine Geodesy*, 45, <https://doi.org/10.1080/01490419.2021.2011502>, 2022.

1010 Weiss, J. and Bernardara, P.: Comparison of local indices for regional frequency analysis with an  
1011 application to extreme skew surges, *Water Resources Research*, 49,  
1012 <https://doi.org/10.1002/wrcr.20225>, 2013.

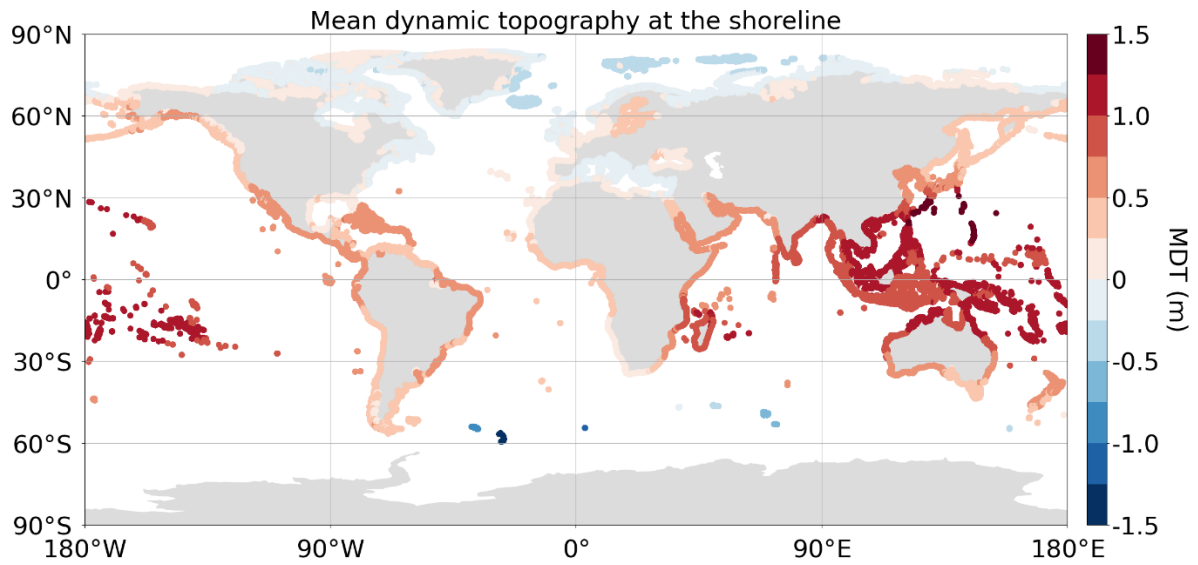
1013 Yang, Z., Wang, T., Castrucci, L., and Miller, I.: Modeling assessment of storm surge in the Salish Sea,  
1014 *Estuarine, Coastal and Shelf Science*, 238, <https://doi.org/10.1016/j.ecss.2019.106552>, 2020.

1015

1016 8. Appendix

1017



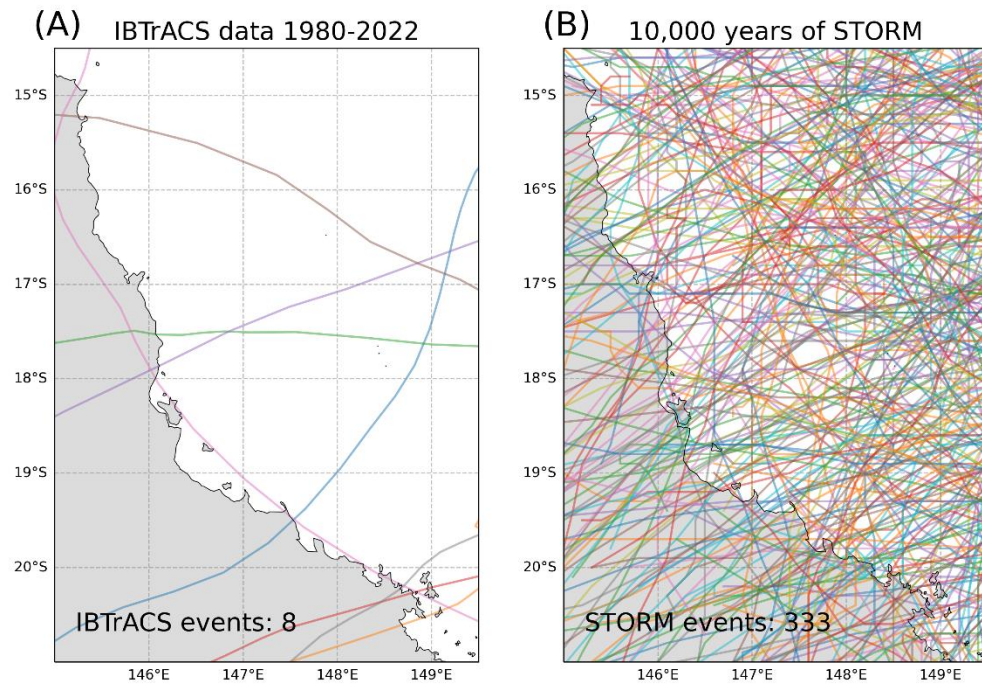


1018

1019  
1020

Figure A1: HYBRID-CNES-CLS18-CMEMS2020 MDT dataset from (Mulet et al., 2021), extracted at the shoreline for use in correcting the output from the RFA for future uses such as inundation modelling.

### Category 4 and 5 hurricanes along the Queensland coastline

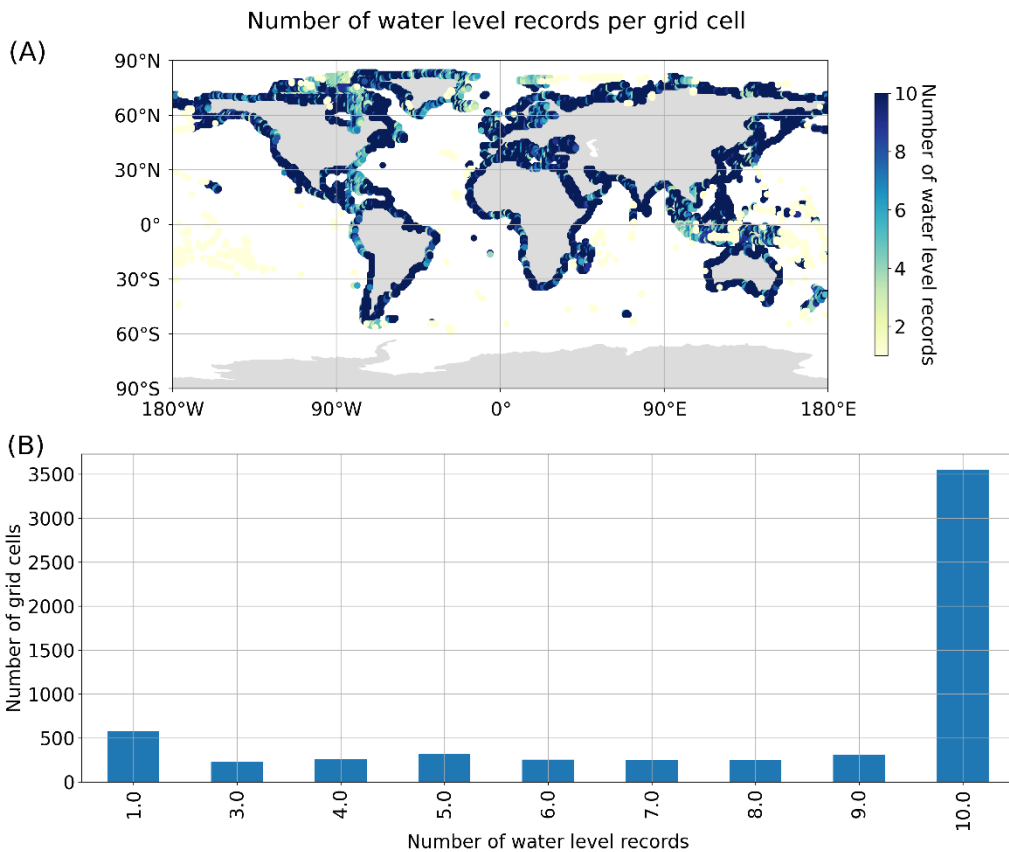


1021

1022  
1023

Figure A2: (A) Category 4 and 5 IBTrACS hurricane impacting the Queensland coastline between 1980-2022 (Knapp et al., 2010) and (B) equivalent STORM events impacting the same the stretch of coastline (Bloemendaal et al., 2020).

1024



1025

1026 *Figure A3: The number of water level records used per grid cell (A) as a scatter plot showing the distribution globally, and*  
 1027 *(B) as a bar plot showing the number of water level records vs the number of grid cells.*

1028

## 1029 9. Code Availability

1030 The Python scripts used for handling the GESLA dataset can be downloaded for:

1031 <https://github.com/philiprt/GeslaDataset>

1032 The Conda package (Python) used for creating the FES2014 tidal timeseries can found at:

1033 <https://anaconda.org/fbriol/pyfes>

## 1034 10. Data availability

1035 GESLA tide gauge data is available at: <https://gesla787883612.wordpress.com/downloads/>

1036 GTSM data is available at: <https://cds.climate.copernicus.eu/cdsapp#!/dataset/sis-water-level-change-timeseries?tab=overview>

1038 ERA5 wave hindcast data is available at:

1039 <https://cds.climate.copernicus.eu/cdsapp#!/dataset/reanalysis-era5-single-levels?tab=overview>

1040 FES2014 tidal heights can be downloaded from:

1041 <https://www.aviso.altimetry.fr/en/data/products/auxiliary-products/global-tide-fes.html>

1042 HYBRID-CNES-CLS18-CMEMS2020 is available at:

1043 <https://www.aviso.altimetry.fr/en/data/products/auxiliary-products/mdt/mdt-global-hybrid-cnescs-cmems.html>  
1044

1045 Copernicus 30m DEM is found at: <https://spacedata.copernicus.eu/collections/copernicus-digital-elevation-model>  
1046

1047 COAST-RP dataset is downloaded from: [https://data.4tu.nl/articles/\\_/13392314](https://data.4tu.nl/articles/_/13392314)

1048 The data produced in this study is available for academic, non-commercial research only. Please  
1049 contact the corresponding author for access.

## 1050 11. Author contributions

1051 T.C. was responsible for coding up the pre-processing the tide gauge and GTSM data, coding up the  
1052 RFA and validating the results. N.Q. pre-processed the wave data, including fitting the copula to  
1053 predict wave conditions for tide gauge records that extended beyond the hindcast period. J.G.  
1054 created the coastline output points using the Copernicus DEM. I.P. worked on the evaluating the  
1055 empirical shape parameter limiter. H.W. assisted in validating the output results from the RFA. S.M.  
1056 supplied the GTSM dataset and W.S. provided the RFA methodology which we applied globally. I.H.  
1057 and P.B. provided guidance and assistance throughout. T.C. prepared the manuscript with  
1058 contributions and editing from all co-authors.

## 1059 12. Competing Interests

1060 The authors declare that they have no conflict of interest.